Taylor & Francis
Taylor & Francis Group

RESEARCH PAPER

🔓 OPEN ACCESS   ✓ Check for updates

Nonreceptor tyrosine kinase ABL1 regulates lysosomal acidification by phosphorylating the ATP6V1B2 subunit of the vacuolar-type H⁺-ATPase

Caiwei Song[a]*, Qincai Dong[a]*, Yi Yao[a], Yan Cui[a], Chunmei Zhang[b], Lijun Lin[a], Lin Zhu[a], Yong Hu[a], Hainan Liu[a], Yanwen Jin[a], Ping Li[a], Xuan Liu[a], and Cheng Cao[a]

[a]State Key Laboratory of Pathogen and Biosecurity, Beijing Institute of Biotechnology, Beijing, China; [b]Shanghai Key Laboratory of Regulatory Biology, Institute of Biomedical Sciences and School of Life Sciences, East China Normal University, Shanghai, China

ABSTRACT

The vacuolar-type H⁺-ATPase (V-ATPase) is a proton pump responsible for controlling the intracellular and extracellular pH of cells. Its activity and assembly are tightly controlled by multiple pathways, of which phosphorylation-mediated regulation is poorly understood. In this report, we show that in response to starvation stimuli, the nonreceptor tyrosine kinase ABL1 directly interacts with ATP6V1B2, a subunit of the V_1 domain of the V-ATPase, and phosphorylates ATP6V1B2 at Y68. Y68 phosphorylation in ATP6V1B2 facilitates the recruitment of the ATP6V1D subunit into the V_1 subcomplex of V-ATPase, therefore potentiating the assembly of the V_1 subcomplex with the membrane-embedded V_0 subcomplex to form the integrated functional V-ATPase. ABL1 inhibition or depletion impairs V-ATPase assembly and lysosomal acidification, resulting in an increased lysosomal pH, a decreased lysosomal hydrolase activity, and consequently, the suppressed degradation of lumenal cargo during macroautophagy/autophagy. Consistently, the efficient removal of damaged mitochondrial residues during mitophagy is also impeded by ABL1 deficiency. Our findings suggest that ABL1 is a crucial autophagy regulator that maintains the adequate lysosomal acidification required for both physiological conditions and stress responses.

Abbreviation: ANOVA: analysis of variance; Baf A1: bafilomycin A1; CCCP: carbonyl cyanide 3-chlorophenylhydrazone; CRK: CRK proto-oncogene, adaptor protein; CTSD: cathepsin D; DMSO: dimethylsulfoxide; EBSS: Earle's balanced salt solution; FITC: fluorescein isothiocyanate; GFP: green fluorescent protein; GST: glutathione S-transferase; LAMP2: lysosomal associated membrane protein 2; MAP1LC3/LC3: microtubule associated protein 1 light chain 3; MTORC1: mechanistic target of rapamycin kinase complex 1; PD: Parkinson disease; PLA: proximity ligation assay; RFP: red fluorescent protein; WT: wild-type.

Introduction

The V-ATPase is an ATP-driven proton pump embedded in various intracellular membranes, such as the membranes of endosomes and lysosomes, and the plasma membrane of specialized cell types [1]. It hydrolyzes ATP and drives H⁺ into the lumen, establishing a more than 100-fold H⁺ concentration gradient across membranes to form and maintain an acidic internal environment [1,2]. The V-ATPase plays important roles in autophagy [3], cell signaling [4], aging and neurodegenerative diseases [5], the coupled transport of small molecules and entry of various viruses and toxins [6].

The V-ATPase is tightly controlled in cells as a crucial regulator of intracellular pH homeostasis. Like F-type and A-type ATPases, V-ATPases are large multi-subunit complexes consisting of a peripheral V_1 domain for ATP hydrolysis and a transmembrane V_0 domain for transporting protons [7,8]. ATP hydrolysis by cytoplasmic V_1 ATPase drives the rotation of the membrane-embedded, ring-shaped V_0 proton pump to allow cycles of protonation and deprotonation of lipid-exposed glutamic acid residues for coupled proton transfer [8–10]. V-ATPase activity in cells is tightly regulated by the reversible dissociation of the V_1 domain from the V_0 domain in response to various stimuli, such as growth factor stimulation, nutrient cues, and cellular differentiation [11–13]. Glucose deprivation results in the release of V_1 subunits into the cytosol and abnormal organelle acidification [14–16], and amino acid starvation increases both V-ATPase assembly and V-ATPase-dependent lysosomal acidification [17,18]. The dysregulation of V-ATPases can lead to impaired lysosomal acidification, causing the aberrant accumulation of its substrates, and has been implicated in numerous diseases, including neurodegenerative disorders, cancer, and metabolic disorders [19–22]. The underlying mechanism responsible for V-ATPase regulation remains unclear.

Autophagy is an evolutionarily conserved stress-responsive process that contributes to the clearance of superfluous or potentially dangerous proteins and organelles by

---

🅒 Supplemental data for this article can be accessed online at https://doi.org/10.1080/15548627.2024.2448913

lysosomes, which are intracellular digestive organelles containing various acid hydrolases [23–28]. V-ATPases play essential roles in autophagy by maintaining a unique low internal pH of 4.5–5.0 in the lysosome, and facilitate the fusion of autophagosomes with lysosomes to form autolysosomes and the subsequent degradation of the intralumenal contents [29,30]. ABL1 (ABL proto-oncogene 1, non-receptor tyrosine kinase), a kinase activated by several stress stimuli, is involved in the regulation of the autophagy-lysosome pathway [31,32]. The administration of the ABL1 inhibitors imatinib and nilotinib can inhibit the activity and mature of lysosomal hydrolases [33], induce autophagy in chronic myeloid leukemia (CML) cells [34] or rescue autophagy-lysosome pathway dysfunction and reduce the accumulation of the related substrates Aβ or α-synuclein in abnormally activated ABL1 cells or disease models [35].

In this study, we found that ABL1 colocalized with V-ATPase under starvation conditions. The ATP6V1B2 subunit of V-ATPase was confirmed to be a new substrate for the kinase ABL1, and ABL1-mediated ATP6V1B2 phosphorylation was shown to play important roles in the assembly of functional V-ATPase and the lysosomal acidification.

Results

ABL1 kinase interacts with the ATP6V1B2 subunit of V-ATPase

Nonreceptor tyrosine kinase ABL1 is activated by numerous stress stimuli, such as ionizing radiation, oxidative stress, and starvation. In our earlier investigation, ABL1 was activated by starvation (Figure S1A) and was observed to be localized in the lysosome in response to starvation stimulation (Figure 1A). Next, the lysosomal proteins bearing phosphorylated tyrosines were searched against the PhosphoSitePlus database (www.phosphosite.org), and several subunits of V-ATPase, such as ATP6V1A and ATP6V0D1, were found to contain phosphorylated tyrosine residues (Figure S1B). Flag-ATP6V0D1 coexpressed with ABL1 in HEK293 cells was subjected to immunoprecipitation with an anti-Flag antibody to determine the potential ABL1 substrate in the V-ATPase. The immunoprecipitates containing Flag-ATP6V0D1 and associated proteins were resolved by SDS-PAGE and immunoblotted with an anti-p-Tyr antibody. Flag-ATP6V0D1 and a larger ~ 55 kDa protein, which was suggested to be the ATP6V1B2 subunit of V-ATPase by the subsequent LC-MS/MS analysis (Figure S1C), were phosphorylated in the presence of wild-type ABL1 but not the dominant negative ABL1^{K290R} (Figure 1B). Tyrosine phosphorylation of these two proteins was significantly inhibited by the selective ABL1 inhibitor nilotinib (Figure 1B). Considering the substantially higher level of overexpressed ATP6V0D1 than the coprecipitated endogenous ATP6V1B2 protein (Figure S1D), the ATP6V1B2 was more prone to be phosphorylated by ABL1.

Next, A549 cell extracts were subjected to anti-ABL1 (or IgG as a control) immunoprecipitation, and the precipitates were immunoblotted with an anti-ATP6V1B2 antibody to substantiate the association of ATP6V1B2

with ABL1. ATP6V1B2 was present in anti-ABL1 (but not IgG) immunoprecipitates, indicating the association of endogenous ABL1 with ATP6V1B2 (Figure 1C). The ABL1-ATP6V1B2 interaction was potentiated by starvation, and the starvation-potentiated association was significantly suppressed by nilotinib, which suggested that the interaction was at least partially dependent on ABL1 activity (Figure 1C). Reciprocal immunoprecipitation analysis also supported this interaction (Figure 1D). The ABL1-ATP6V1B2 interaction was subsequently observed in HeLa cells (Figure S1E) and HEK293 cells overexpressing ABL1 and ATP6V1B2 (Figure 1E). Moreover, the endogenous ABL1 was observed to colocalize with ATP6V1B2 in A549 cells following starvation (Figure S1F), which was further confirmed in cells via an *in situ* proximity ligation assay (PLA). The proximity ligation signal was significantly enhanced by starvation and suppressed by nilotinib treatment (Figure 1F). In addition, the results of staining for lysosomal marker LAMP2 revealed that the ATP6V1B2-ABL1 interaction occurred in the cytosol, rather than in lysosomes (Figure S1G). These results collectively demonstrated that ABL1 interacted with the ATP6V1B2 subunit of the V-ATPase, and the interaction was potentiated in response to starvation stimuli in a kinase activity-dependent manner.

Binding of ABL1 to the ATP6V1B2 subunit of the V-ATPase

Lysates from cells coexpressing ATP6V1B2-Flag and MYC-ABL1 were incubated with GST-ABL1 SH2-, GST-ABL1 SH3-, or GST-conjugated agarose beads *in vitro* to further delineate the interaction between ABL1 and ATP6V1B2. An analysis of the absorbates via anti-Flag immunoblotting revealed that ATP6V1B2-Flag interacted with the ABL1 SH2 domain (Figure 2A) but the protein exhibited far less binding to the ABL1 SH3 domain (Figure 2A). Then, immunoprecipitates of ATP6V1B2-Flag coexpressed with ABL1 were treated with or without phosphatase, resolved on SDS-PAGE gels and transferred to PVDF membranes. Blots of GST-ABL1 SH2 demonstrated that the ABL1 SH2 domain interacted with ATP6V1B2 directly, which was greatly attenuated by phosphatase treatment. This finding suggested that ABL1 SH2 interacted with phosphorylated tyrosines in ATP6V1B2 (Figure 2B). In concert with the results of the GST affinity-isolation experiments, no detectable direct interaction between ABL SH3 and ATP6V1B2 was observed.

Furthermore, ATP6V1B2 truncants were constructed based on the functional domains (Figure 2C). The results showed that both ATP6V1B2(Δ1–49)-Flag and ATP6V1B2 (Δ1–172)-Flag failed to interact with MYC-ABL1, suggesting that aa 1–49 of ATP6V1B2 are indispensable for the interaction with ABL1 (Figure 2D). Although the direct binding between ABL1 SH3 and ATP6V1B2 was difficult to detect by *in vitro* assay (Figure 2A, B), the mutation of ATP6V1B2 P15, P18, which was predicted to be a characteristic ABL1 SH3 binding motif, seriously impaired the ABL1 interaction unexpectedly (Figure 2E).
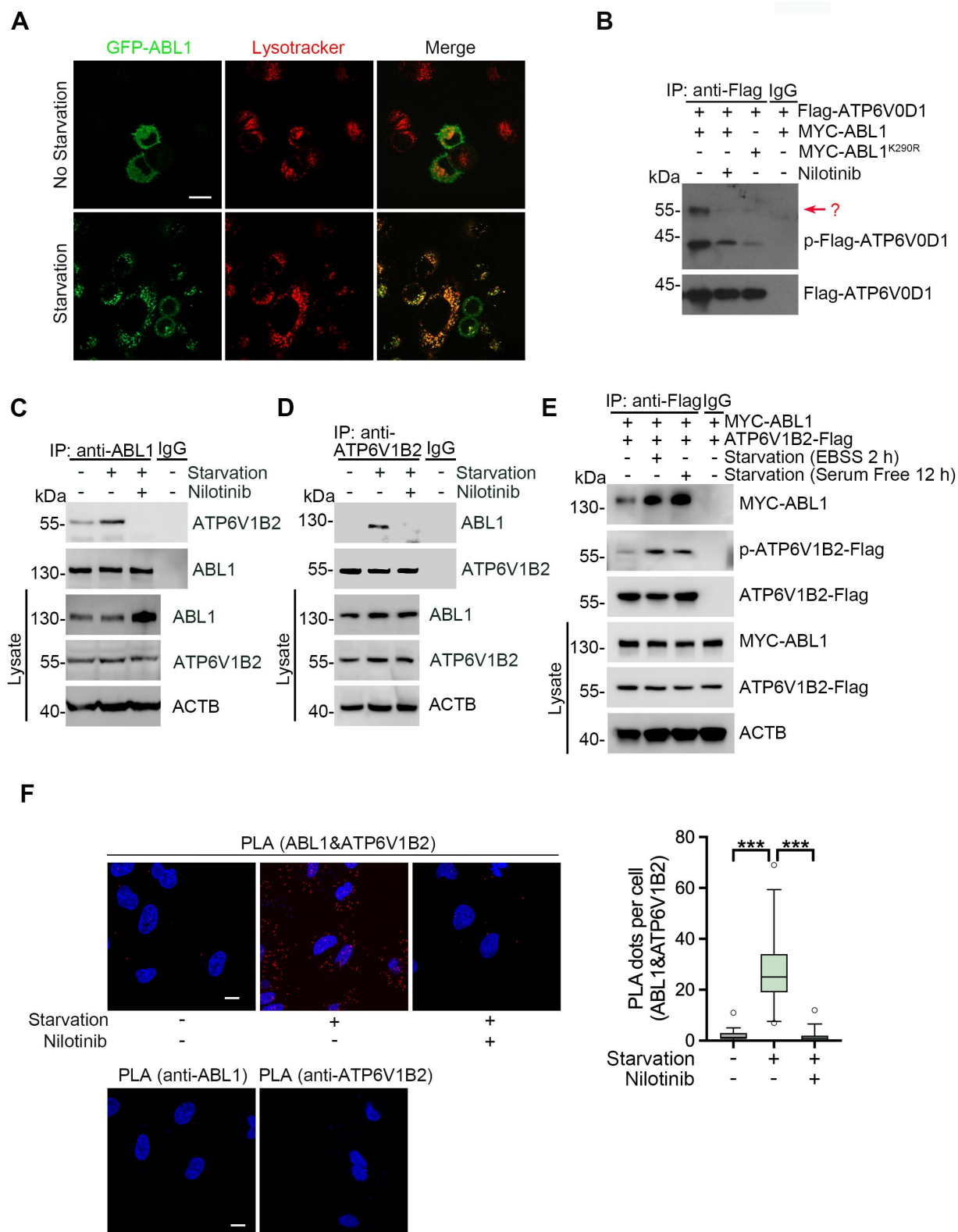
Figure 1. Association of ATP6V1B2 with ABL1. (A) starved HeLa cells (EBSS, 4 h) expressing GFP-ABL1 were stained with LysoTracker and detected via fluorescence microscopy (scale bar: 10 μm). (B) lysates of HEK293 cells coexpressing flag-ATP6V0D1 and MYC-ABL1 or MYC-ABL1(KR) were subjected to immunoprecipitation with an anti-flag antibody or mouse IgG and immunoblotted with an anti-p-tyr or anti-flag antibody. (C and D) A549 cells treated with 10 μM nilotinib or DMSO for 12 h were subjected to starvation (EBSS, 1 h). Lysates were immunoprecipitated with an anti-ABL1 antibody (C), an anti-ATP6V1B2 antibody (D) or mouse IgG and analyzed by immunoblotting. (E) HEK293 cells subjected to the indicated treatments were analyzed by immunoprecipitation and immunoblotting. (F) A549 cells subjected to the indicated treatments were subjected to an *in situ* PLA assay with both anti-ABL1 and anti-ATP6V1B2 antibodies or only one antibody (red, scale bar: 10 μm), images were quantified using ImageJ and plotted in the right panel ($n = 50$–60, one-way ANOVA with Tukey's test for multi-groups and multiple tests, ***$p < 0.001$). At least three independent replicates of all experiments, except for those shown in B, were performed.
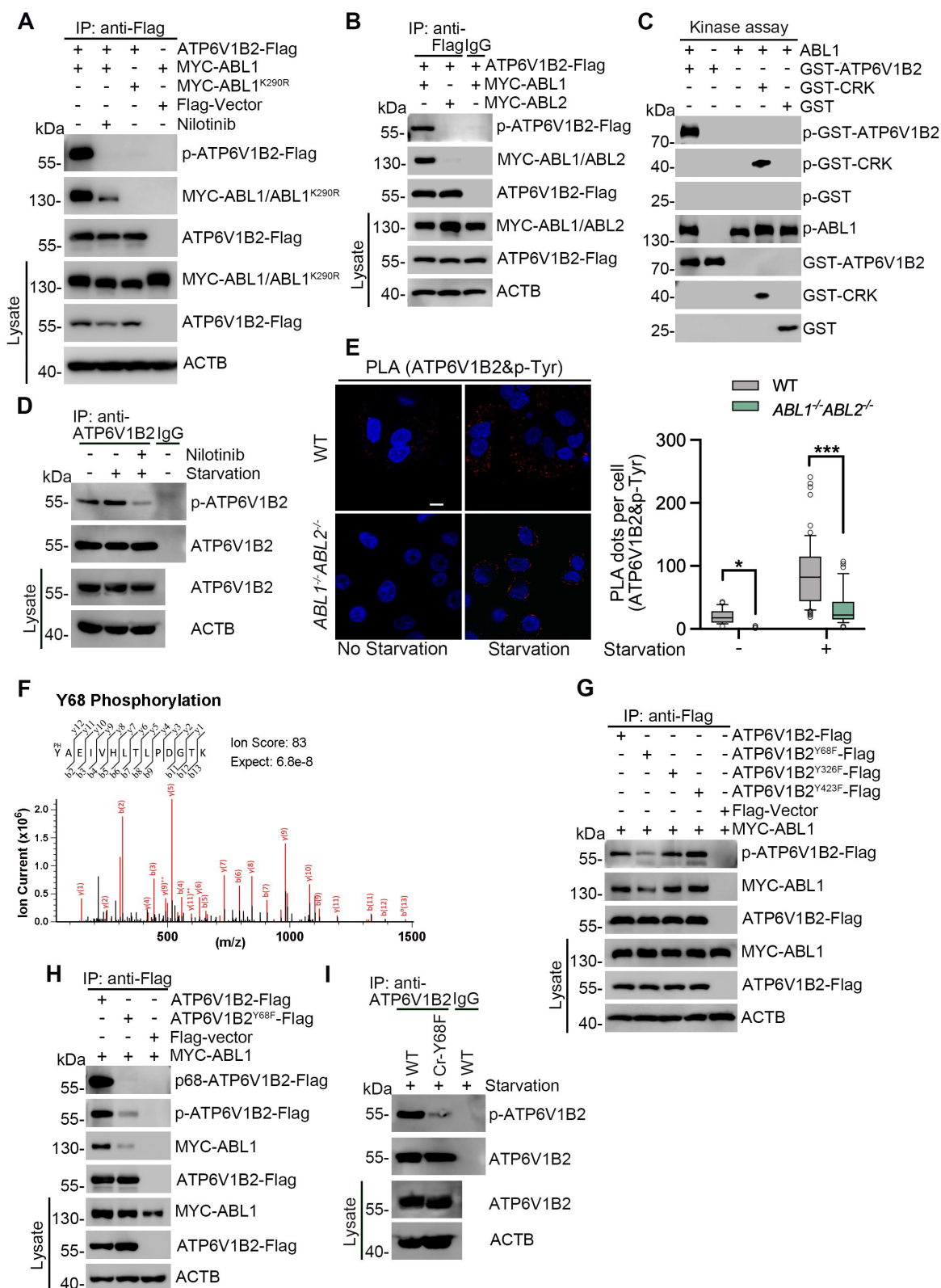
Figure 2. ABL1 directly interacts with ATP6V1B2. (A) lysates from HEK293 cells cotransfected with ATP6V1B2-flag and MYC-ABL1 were incubated with equal amounts of sepharose beads conjugated to the GST-ABL1-SH3/SH2 fusion protein or GST only. The absorbates were analyzed by immunoblotting and Coomassie brilliant blue staining. (B) anti-flag or anti-IgG immunoprecipitates prepared from HEK293 cells that were transfected and treated as indicated were resolved on SDS-PAGE gels, transferred onto PVDF membranes, and blotted with eluted GST-ABL1-SH3/SH2 or GST as a control. The membrane-bound GST tag was detected via anti-gst immunoblotting. (C) the primary structure of ATP6V1B2 predicted by InterPro. (D and E) lysates of HEK293 cells transfected with the indicated plasmids were analyzed by immunoprecipitation and immunoblotting. At least three independent replicates of all experiments were performed.

These results suggested that both the SH3 domain and the SH2 domain are required for ATP6V1B2 binding, and that the SH2 domain might tendentiously directly bind to the phosphorylated tyrosine(s) of ATP6V1B2.

ABL1 phosphorylates the ATP6V1B2 subunit of V-ATPase

ATP6V1B2 interacted with kinase-active ABL1 primarily through the SH2 domain (Figures 1C, 2A, B), suggesting that ATP6V1B2 is a substrate of ABL1. Starvation potentiated

Figure 3. ABL1 phosphorylated ATP6V1B2 at Y68. (A and B) lysates of HEK293 cells transfected with the indicated plasmids were immunoprecipitated with anti-flag beads and analyzed by immunoblotting. (C) *in vitro* kinase assay. Recombinant ABL1 was incubated with GST-CRK, GST-ATP6V1B2 or GST at 30°C for 30 min in the presence of 1 mm ATP. The reaction products were analyzed by SDS-PAGE and immunoblotting. (D) lysates of A549 cells treated with 10 μM nilotinib or DMSO for 12 h were starved with EBSS for 1 h, and the lysates were analyzed by immunoprecipitation and immunoblotting with the indicated antibodies. (E) WT cells and *ABL1^{-/-} ABL2^{-/-}* A549 cells that were starved (EBSS, 1 h) or not starved were subjected to an *in situ* PLA assay with anti-ATP6V1B2 and anti-p-tyr antibodies (red, scale bar: 10 μm). The plots show the quantification of ATP6V1B2-p-tyr interaction complexes in each cell, as analyzed using ImageJ (*n* = 60–100 cells, two-way ANOVA with Tukey's test for more than two groups and multiple tests, ***p < 0.001). (F) ATP6V1B2-flag coexpressed with MYC-ABL1 were purified via immunoprecipitation with an anti-flag antibody and the immunoprecipitates were resolved on SDS-PAGE gels and then stained with Coomassie Brilliant Blue. The ~ 55 kDa band was excised and subjected to trypsin digestion and LC-MS/MS analysis. Monophosphorylated peptides containing PO₃-modified Y68 were identified. (G and H) lysates of HEK293 cells transfected with the indicated plasmids were immunoprecipitated with anti-flag beads and analyzed by immunoblotting. (I) lysates of starved WT or Cr-Y68F A549 cells were immunoprecipitated with an anti-ATP6V1B2 antibody or IgG and analyzed by immunoblotting. At least three independent replicates of all experiments, except for those shown in F, were performed.

the tyrosine phosphorylation of ATP6V1B2 in HEK293 cells overexpressing MYC-ABL1 and ATP6V1B2 (Figure 1E). As shown in Figure 3A, tyrosine phosphorylation of ATP6V1B2-Flag was observed following the expression of MYC-ABL1 but not dominant-negative ABL^{K290R} (Figure 3A). MYC-ABL1-mediated phosphorylation of ATP6V1B2 was significantly attenuated by nilotinib treatment (Figure 3A). In contrast, no detectable ATP6V1B2-Flag phosphorylation was detected in cells expressing MYC-ABL2, which is 90% homologous to ABL1 in the kinase domain, consistent with the considerably weak interaction between ABL2 and ATP6V1B2 (Figure 3B). Purified GST-ATP6V1B2 (but not GST) was directly phosphorylated by recombinant ABL1 via *in vitro* tyrosine kinase assay, similar to the positi*v*e control ABL1 substrate CRK (Figure 3C). Moreover, the endogenous ATP6V1B2 in A549 cells was tyrosine phosphorylated, which was potentiated by starvation and significantly suppressed by nilotinib treatment (Figure 3D) or by CRISPR-mediated ABL1 ABL2 double depletion, as observed using a PLA with anti-p-Tyr and anti-ATP6V1B2 antibodies (Figures 3E and S2A-S2C). In combination with the findings that the P$_{15}$ELP$_{18}$ motif was indispensable for the interaction, tyrosine phosphorylation of ATP6V1B2 potentiated by starvation was attenuated by the P15, 18A mutation (Figure 2E, 2nd panel).

Next, ATP6V1B2-Flag coexpressed with MYC-ABL1 in HEK293 cells was immunoprecipitated with anti-Flag beads and resolved on SDS-PAGE gels. The Coomassie Blue-stained gel containing ATP6V1B2-Flag was subjected to LC-MS/MS. Three tyrosine phosphorylation sites, pY68, pY326 and pY423 were revealed with ion scores > 50 (Figures 3F and S2D). Then, wild-type or Y-to-F mutated ATP6V1B2-Flag was coexpressed with MYC-ABL1 and analyzed by immunoprecipation and immunoblotting. Compared with wild-type ATP6V1B2, ATP6V1B2^{Y68F} exhibited clearly attenuated tyrosine phosphorylation (Figure 3G), indicating that Y68 was the major phosphorylation site. Furthermore, an antibody that specifically recognizes phosphorylated Y68 was developed, and it could specifically react with the peptide containing phosphorylated Y68 (Figure S2E). As expected, only wild-type ATP6V1B2, but not ATP6V1B2^{Y68F}, was recognized by the anti-p-Y68 antibody (Figure 3H). The ATP6V1B2^{P15,18A} mutant also showed an attenuated reactivity to the anti-p-Y68 antibody (Figures 2E, 3rd panel). Next, CRISPR-mediated gene editing was used to introduce a homozygous mutation into the ATP6V1B2 genomic loci, which resulted in the expression of a Y to F mutation at amino acid 68 in ATP6V1B2 (the cell line was named as Cr-Y68F) (Figure S2F). Consistent with the findings of the overexpression experiments, the tyrosine phosphorylation of endogenous ATP6V1B2 in Cr-Y68F cells was significantly lower than that in WT cells (Figure 3I). Collectively, these results indicated that the ATP6V1B2 of V-ATPase was phosphorylated primarily at Y68 by ABL1, and possibly by ABL2 to a far lesser extent because of the detectable ABL2-ATP6V1B2 association.

ABL1-mediated ATP6V1B2 phosphorylation promotes V-ATPase assembly

The assembly of the V-ATPase V$_1$ and V$_0$ domains is reversible and regulated by signals such as glucose deprivation [36]. The colocalization of ATP6V1B2 with lysosomes was detected by immunofluorescence staining with antibodies against ATP6V1B2 and LAMP2 to investigate whether the assembly of V-ATPase was regulated by ABL1-mediated phosphorylation of ATP6V1B2. Compared with that in wild-type cells, a substantially lower proportion of the ATP6V1B2 subunit was colocalized with lysosomes in the Cr-Y68F and ABL1-ABL2-depleted cells in response to starvation, indicating that impaired V-ATPase assembly caused by a deficient Y68F phosphorylation in ATP6V1B2 was mediated by ABL1 and ABL2 (Figures 4A and S3A). Next, lysates of starved wild-type and Cr-Y68F cells were subjected to immunoprecipitation with an anti-ATP6V1B2 antibody. An analysis of the immunoprecipitates showed that the ATP6V1D and ATP6V1A proteins were present at lower levels in the ATP6V1B2 immunoprecipitates of Cr-Y68F cells (Figure 4B). Inhibition of ABL1 with nilotinib also resulted in a decreased ATP6V1B2-ATP6V1D interaction in response to starvation (Figures 4C, 1st panel, and S3B). Then, the ATP6V1B2-ATP6V1D association was further accessed via an *in vitro* binding assay. ATP6V1B2-Flag or ATP6V1B2^{Y68F}-Flag coexpressed with MYC-ABL1 was precipitated with an anti-Flag antibody, treated with/without phosphatase, washed 3 times with high-salt buffer and eluted by Flag peptides substitution. Eluted ATP6V1B2 was then incubated with recombinant His-ATP6V1D and then subjected to immunoprecipitation with anti-Flag. An analysis of the adsorbents by immunoblotting revealed that far less ATP6V1D was present in the phosphatase-treated wild-type ATP6V1B2 or ATP6V1B2^{Y68F} immunoprecipitates (Figure 4D, E). These results collectively showed that the ABL1-mediated phosphorylation of Y68 in ATP6V1B2 regulates the ATP6V1B2-ATP6V1D interaction and consequently the assembly of the functional V1 domain.

The V$_1$ domain docks onto the membrane-embedded V$_0$ domain via its central rotor, which is composed of ATP6V1D and ATP6V1F, with the ring of V$_0$ composed of ATP6V0C [37,38]. In concert with the weakened V$_1$ domain assembly, the V$_1$-V$_0$ association was also impaired in Cr-Y68F cells. Compared with that in wild-type cells, significantly less ATP6V1B2 was detected in the anti-ATP6V0D1 immunoprecipitates of Cr-Y68F cells (Figure 4F). Accordingly, the starvation-induced V$_1$-V$_0$ interaction, as indicated by the ATP6V1B2-ATP6V0D1 interaction in the PLA assay, was suppressed by nilotinib, ABL1 ABL2 depletion, or the Y68F mutation in ATP6V1B2 (Figures 4G and S3C). Moreover, the Y68F mutation or ABL1 inhibition resulted in significantly reduced ATP6V1B2 levels (>50%) in lysosomal extracts prepared from starved cells (Figures S3D-S3E). These results demonstrated that the ABL1-mediated phosphorylation of Y68 in ATP6V1B2 in response to starvation potentiates the ATP6V1B2-ATP6V1D interaction and thereby facilitates V$_1$ domain docking to the V$_0$ domain.
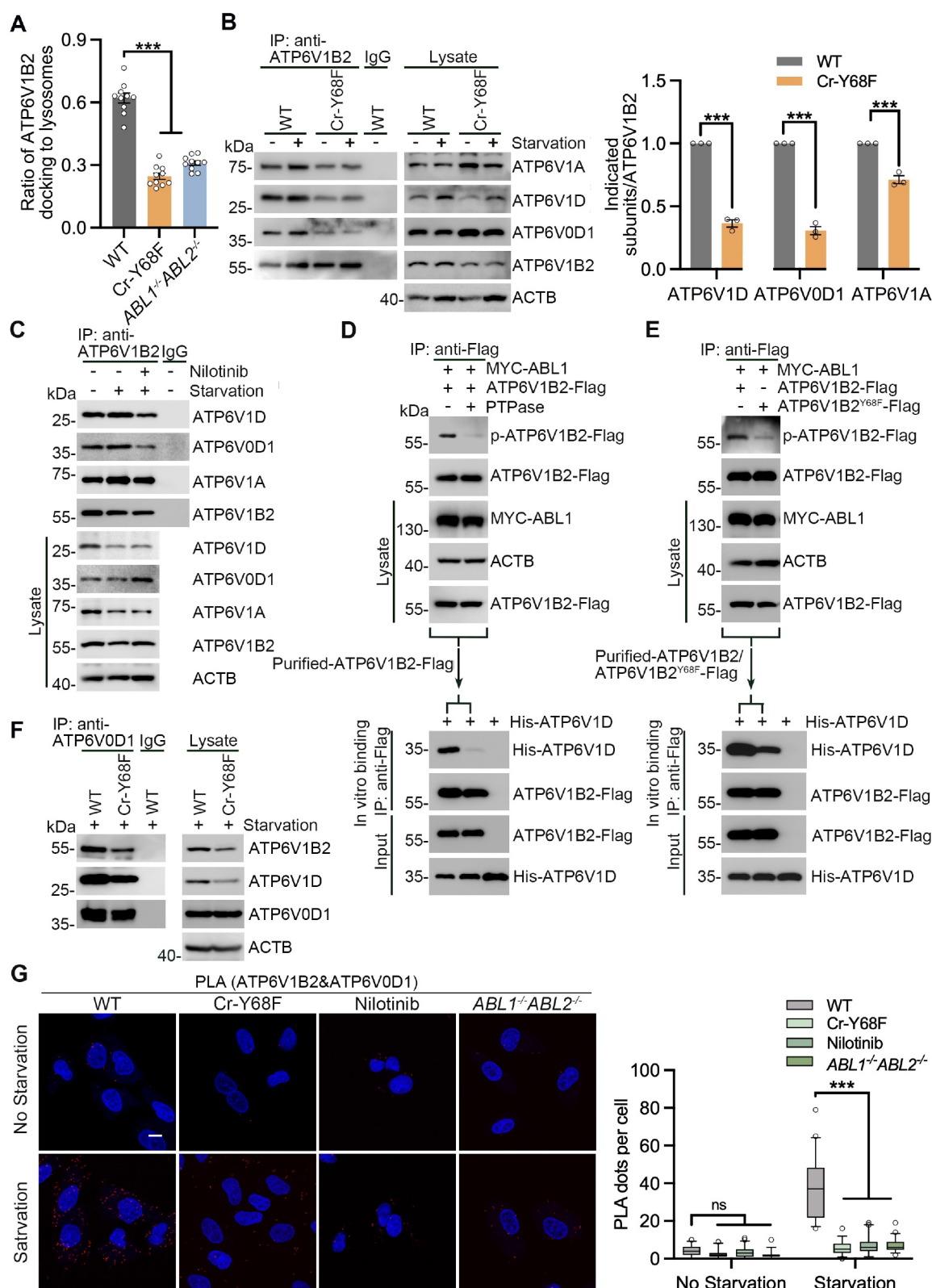
Figure 4. ABL1-mediated phosphorylation of ATP6V1B2 potentiates the assembly of V-ATPase. (A) WT, Cr-Y68F and *ABL1⁻ᐟ⁻ ABL2⁻ᐟ⁻* A549 cells subjected to the indicated treatments were stained with anti-ATP6V1B2 and anti-LAMP2 antibodies (figure S3A). The ratio of ATP6V1B2 docking to lysosomes in starved cells was quantified using ImageJ and plotted (n = ten randomly selected fields, each dot contains at least 5 cells, one-way ANOVA with Tukey's test for multi-groups and multiple tests, ***$p < 0.001$). (B) left panel, lysates of starved or no starved WT or Cr-Y68F A549 cells, were immunoprecipitated with an anti-ATP6V1B2 antibody or IgG and analyzed by immunoblotting. Right panel, bar plots show the quantification of the levels of indicated proteins in starved cells using ImageJ (n = 3, two-way ANOVA with Tukey's test for multi-groups and multiple tests, ***$p < 0.001$). (C) lysates of A549 cells treated as indicated were immunoprecipitated with an anti-ATP6V1B2 antibody or IgG and analyzed by immunoblotting. (D and E) lysates of starved HEK293 cells cotransfected with the indicated plasmids and treated with/ without PTPase were subjected to anti-flag immunoprecipitation. Then, the flag-tagged ATP6V1B2 was eluted from the beads with the flag peptide, and incubated with 2 μg of his-V1D for 30 min. The mixture was subjected to immunoprecipitation with anti-flag beads followed by immunoblotting with the indicated antibodies. (F) lysates of starved WT or Cr-Y68F A549 cells were immunoprecipitated with an anti-ATP6V0D1 antibody or IgG and analyzed by immunoblotting. (G) WT, Cr-Y68F

ABL1-mediated ATP6V1B2 phosphorylation is required for the maintenance of lysosomal pH homeostasis

ABL1-mediated Y68 phosphorylation contributed to the assembly of the functional V-ATPase, suggesting that ABL1 is involved in the regulation of V-ATPase activity and lysosomal pH via ATP6V1B2 phosphorylation. As expected, lysosomal V-ATPase prepared from Cr-Y68F or *ABL1-ABL2*-depleted cells exhibited an ~60% suppression of V-ATPase activity compared with lysosomal V-ATPase prepared from wild-type cells (Figure 5A). Moreover, when live cells were stained with a pH-sensitive dye (LysoTracker™ Red DND-99), a substantially compromised staining intensity was observed in Cr-Y68F as well as *ABL1-ABL2*-null cells or *ABL1*-knockout cells, compared with wild-type cells, suggesting that cells expressing ATP6V1B2 deficient in Y68 phosphorylation have inefficient V-ATPase activity and therefore a hypoacidified lysosomal environment (Figures 5B, S4A and S4B).

To further investigate how lysosomal acidification is regulated by Y68 phosphorylation, cells were infected with a recombinant lentivirus expressing the LC3 protein tandemly fused to an acid-insensitive RFP and an acid-sensitive GFP (StubRFP-sensGFP-LC3). In the lysosome, the fluorescence of GFP is quenched due to the low pH, whereas the fluorescence of RFP is stable. Consistent with previous findings, a higher GFP:RFP ratio (indicated by a greener fluorescence) in the lysosomes, which suggests a higher pH or impeded autophagosome-lysosome fusion, was observed in cells treated by asciminib, one of the new generations of ABL1 inhibitors with better specificity (Figures 5C and S4C), as well as in the Cr-Y68F or *ABL1-ABL2*-depleted cells, than in the wild-type cells (Figures 5D and S4D). The unaffected colocalization of LC3 and CTSD (cathepsin D; a lysosomal proteinase) after starvation suggested that ABL1 had little, if any, effect on autophagosome-lysosome fusion, which further supported that the impaired lysosomal acidity and abnormally high pH are responsible for the higher GFP:RFP ratio (Figure S4E). Finally, the lysosomal pH was more accurately determined using the dual-fluorescence probes, including pH-sensitive fluorescein (FITC-dextran) and pH-insensitive tetramethylrhodamine (TMR-dextran) [39]. Compare with the lysosomal pH of 4.5 in wild-type cells, cells bearing ATP6V1B2^{Y68F} mutation (A549 Cr-Y68F) presented significant lysosomal hypoacidity, with an increased pH of approximately 5.3 (Figure 5E). Consistent with this observation, nilotinib treatment also resulted in severe lysosomal hypoacidity in a concentration-dependent manner (Figure 5F).

Consequently, the activation of lysosomal hydrolases such as CTSB (cathepsin B), whose activity depends on the low pH in the lysosome [40,41], was impaired in Cr-Y68F or *ABL1-ABL2*-depleted cells upon starvation compared with that in wild-type cells as determined by Magic Red staining (Figures 5G and S4F), as was the activation of CTSD (cathepsin D), as determined by pepstatin A BODIPY FL specifically binding to the mature CTSD [42] (Figure 5H). Asciminib also reduced the activation of CTSD (Figure 5I). Accordingly, ABL1 activation by DPH facilitated lysosomal acidification, but only in the absence of Baf A1, a potent proton pump inhibitor of V type ATPase [43] (Figures 5J and S5A-S5D).These results collectively suggested that ABL1-mediated phosphorylation of Y68 in ATP6V1B2 played an essential role in maintaining lysosomal pH and pH-dependent lysosomal hydrolases activity by regulating the activity of V-type ATPases.

ATP6V1B2 Y68 phosphorylation deficiency impairs autophagy flux

Considering that inadequate lysosomal acidification and impaired digestion activity may disturb autophagy flux, the accumulation of GFP-LC3 in autophagosomes were accessed. As expected, more GFP-LC3 accumulation was observed under starved or even nonstarved conditions in Cr-Y68F cells, *ABL1-ABL2*-depleted cells, and cells treated with the ABL1 inhibitor asciminib, but to a lesser extent in wild-type A549 cells (Figure 6A, B). Starvation-induced SQSTM1/p62 degradation and low pH-dependent CTSD cleavage and activation were both suppressed by ABL1-ABL2 inhibitors and almost abolished in Cr-Y68F and *ABL1-ABL2*-null cells (Figure 6C, D). Moreover, ABL1 activation promoted autophagy flux and CTSD maturation but had little, if any, effect on the cells treated with the proton inhibitor Baf A1 (Figures S5E and S5F). These data, together with those of the RFP-GFP-LC3 assay shown in Figure 5C, D, demonstrated that ABL1-mediated ATP6V1B2 phosphorylation of Y68 contributed to autophagy flux by regulating the lysosomal degradation capability other than the normal initiation of autophagy.

ABL1-mediated ATP6V1B2 phosphorylation is involved in mitophagy

ABL1 is involved in mitochondrial damage [44,45], and imatinib induces ABL1-dependent mitochondrial damage and cell apoptosis in cardiomyocytes in mouse and human hearts [46–48], which raises the concern that ABL1-mediated ATP6V1B2 phosphorylation is involved in regulating mitochondria degradation in autophagosomes. When cells were exposed to 25 µM nilotinib or 15 µM asciminib, a considerable proportion of mitochondria stained with MitoTracker Deep Red^{FM} colocalized with lysosomes (Figures S6A and S6B), suggesting that ABL1 inhibition may induce the colocalization of mitochondria with lysosomes. Little if any colocalization of mitochondria and lysosomes was observed in the cells bearing the Y68F mutation in ATP6V1B2 (Cr-Y68F) or in the cells depleting ABL1-ABL2 in the absence of a mitophagy-
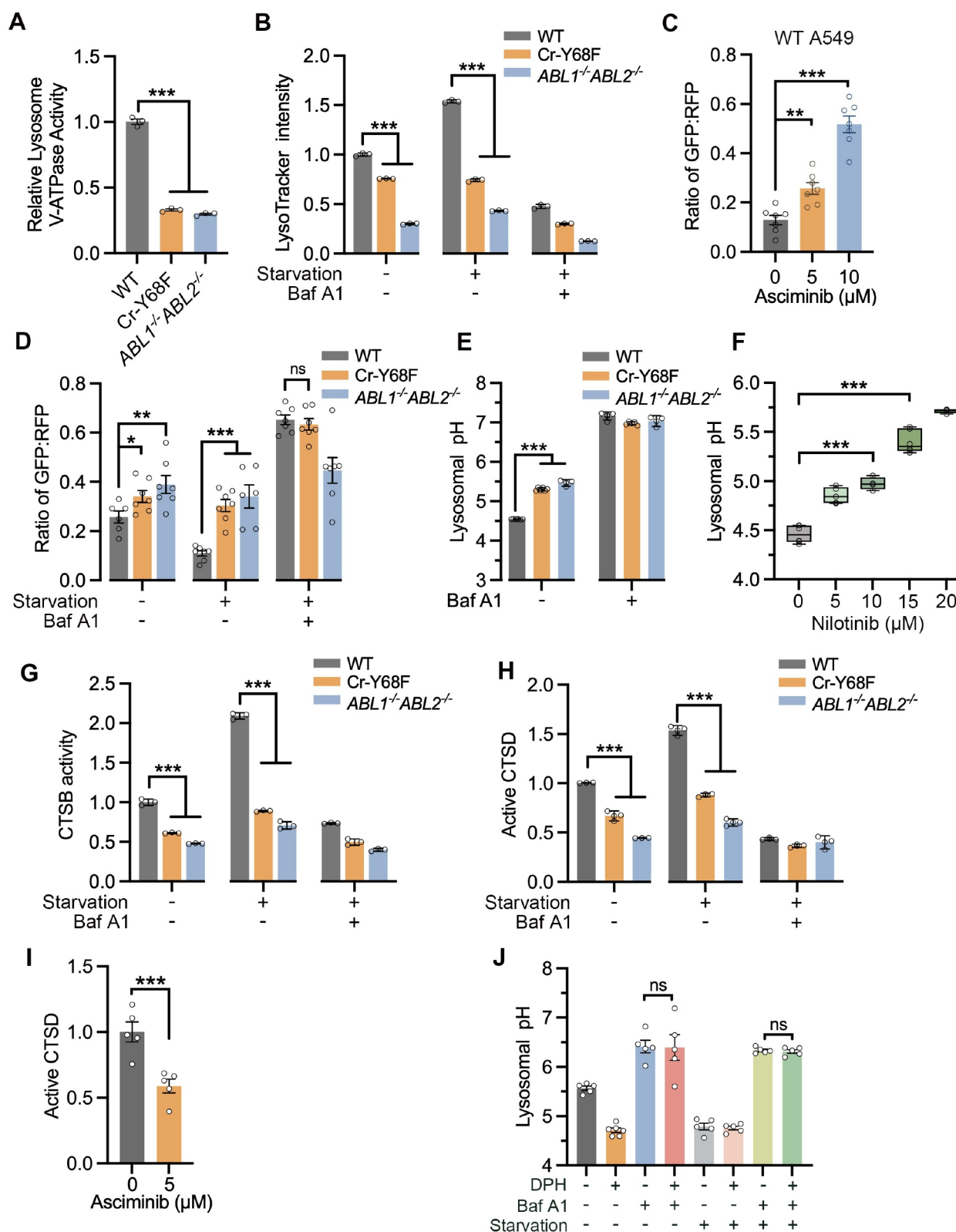
Figure 5. ABL1-mediated ATP6V1B2 phosphorylation regulates lysosomal acidification. (A) the V-ATPase activity of lysosomes isolated from the indicated cell lines was determined, and the results were normalized to the ATP6V0D1 level determined by immunoblotting the lysosome fraction (n = 3, one-way ANOVA with Tukey's test for multi-groups and multiple tests). (B) the fluorescence intensities of LysoTracker staining in WT, Cr-Y68F and *ABL1⁻ᐟ⁻ABL2⁻ᐟ⁻* A549 cells were determined by flow cytometry. The results are presented as the means±s.d.s. Of three independent experiments (each dot represents the average of 10,000 cells), two-way ANOVA with Tukey's test for multi-groups and multiple tests. (C and D) WT, Cr- Y68F or *ABL1⁻ᐟ⁻ABL2⁻ᐟ⁻* A549 cells stably transfected with a puromycin-inducible stubRFP-sensGFP-LC3 lentivirus (MOI = 5) were treated as indicated and detected via immunofluorescence microscopy (figure S4C and D). The GFP:RFP ratio in each field of view was analyzed using ImageJ and plotted (n = 6 (C) or 7 (D), each dot represents a randomly selected image containing at least 10 (C) or 20 (D) cells), one-way ANOVA (C) or two-way ANOVA (D) with Tukey's test for multi-groups and multiple tests. (E) the lysosomal pH in WT, Cr-Y68F and *ABL1⁻ᐟ⁻ABL2⁻ᐟ⁻* A549 cells was determined via flow cytometry using fitc-dextran and tmr-dextran by. Baf-A1 was used as a control (n = 4, each dot represents the average of 10,000 cells; two-way ANOVA with Tukey's test for multi-groups and multiple tests). (F) the lysosomal pH in WT A549 cells treated with nilotinib for 18 h and labeled with fitc-dextran and tmr-dextran, and then

inducing agent (1st row of Figure 7A, B, S6C), which suggested that the deficiency of ATP6V1B2 phosphorylation at Y68 did not induce mitophagy. Then the cells were treated with the mitochondrial protonophore CCCP, which induces mitochondrial depolarization, triggers mitophagy [49] and has little, if any, effect on ABL1 activity, the ABL1-ATP6V1B2 interaction and lysosomal pH (Figures S6D-S6F). A similar amount of mitochondrial matrix (stained with CellLight™ Mitochondrial-GFP (BacMan 2.0)) accumulated in the lysosomes (detected with an anti-LAMP2 antibody) in WT and Cr-Y68F A549 cells treated with CCCP for 1 h (Figures 7A, 2nd row, S6C). Notably, significantly more mitochondria were accumulated within the lysosomes of Cr-Y68F cells compared to the wild-type cells with CCCP for 48 h (Figures 7A, 3rd row, S6C), which suggested that Y68 phosphorylation was involved in the efficient removal of damaged mitochondria by the lysosomes rather than the in initiation of mitophagy. ABL1-regulated mitophagy was further investigated via real-time fluorescence microscopy of stained live cells, and the colocalization of mitochondria with lysosomes was analyzed dynamically. In accordance with the previous findings, no lysosome-colocalized mitochondria were observed in Cr-Y68F cells or ABL1-ABL2-depleted cells, which suggested that ABL1-mediated phosphorylation had little to effect on the initiation of mitophagy (Figures 7B, 1st row). When the cells were treated with CCCP, the ratio of mitochondria retained in mitophagosomes was markedly increased in Cr-Y68F cells and $ABL1^{-/-}$ $ABL2^{-/-}$ cells compared to the wild-type cells. At 48 h after CCCP treatment, the ratio of lysosomal-localized mitochondria increased to ~ 55% in Cr-Y68F and $ABL1^{-/-}$ $ABL2^{-/-}$ cells, whereas the ratio decreased to ~ 10% in wild-type cells (Figure 7B), however, these differences were abolished in the presence of 100 nM Baf A1 (Figure 7B), which increased the lysosomal pH to 5.5. These results suggested that ATP6V1B2 phosphorylation regulating mitophagy by suppressing the final lysosomal degradation of damaged mitochondria but not the initiation of mitophagy and that ABL1 regulates mitophagy primarily by phosphorylating ATP6V1B2 but not other substrates. Moreover, CCC-HEH-2 (human embryonic myocardial tissue derived) cells pretreated with low-dose asciminib or nilotinib showed the significant accumulation of mitochondria in lysosomes after treatment with CCCP (Figure 8A). Mitophagy in starved wild-type, Cr-Y68F and $ABL1^{-/-}$ $ABL2^{-/-}$ cells was then assessed via transmission electron microscopy (TEM). Compared with wild-type cells, classical ruptured, lysosomal embedded mitochondrial membranes were present in Cr-Y68F and ABL1-ABL2-depleted cells (Figure 8B). Consistent with the findings that the administration of imatinib to human and mice resulted in

mitochondrial abnormalities in the cardiomyocytes and cardiac complications [50], the continuous intragastric administration of asciminib, the newest ABL1 inhibitor, resulted in significantly impaired cardiac function (Figure 8C), accompanied by increased colocalization of mitochondria with lysosomes, as shown by LAMP2 and TOMM20 staining (Figure 8D). These results collectively suggested that a deficiency in ATP6V1B2 phosphorylation at Y68 impeded the normal degradation of damaged mitochondria by lysosomes rather than the formation of mitophagosomes, resulting in the accumulation of damaged mitochondria in lysosomes.

Discussion

Lysosomes are the major terminal digestive organelles. The general degradation capability of the lysosome is regulated primarily by its quantity and activity, the latter of which tightly depends on V-ATPase proton pump-mediated lysosomal acidification. V-ATPase is regulated mainly by reversible assembly of the V_0 domain and V_1 domain. NDST3 suppresses V-ATPase assembly on the lysosome and thereby decreases lumen acidification [51], and *MIR1* reduces V-ATPase assembly to sustain muscle physiology [52]. V-ATPase assembly is also regulated by different nutritional conditions. Under amino acid-sufficient conditions, V-ATPase V_1 domains stably exist in the cytosol through an interaction with the chaperonin TRiC. In response to amino acid starvation, the V1 domain moves to lysosomes, assembles with V0 domains into active proton pumps, and acidifies the lysosomal lumen through a PI3K-MTORC1-dependent [53] or PI3K-MTORC1-independent pathway [17].

In this study, for the first time to our knowledge, the V-ATPase was shown to be regulated by a tyrosine phosphorylation. ABL1-mediated ATP6V1B2 phosphorylation plays an essential role in the recruitment of ATP6V1D to generate a complete V1 domain, in turn, the fully assembled and functional V-ATPase (Figure 9). Kinase-mediated phosphorylation of ATP6V1B2 results in the assembly of V-ATPase in response to environmental stimuli, such as nutrient starvation and possibly irradiation or reactive oxidative species, which result in the activation of the ABL kinase, thereby maintaining lysosomal homeostasis and facilitating the degradation of proteins or organelles in the lysosomal lumen. These findings revealed an underlying mechanism responsible for the direct control of lysosomal catabolic activity by the ABL1 kinase as a principle metabolic regulator in mammalian cells.
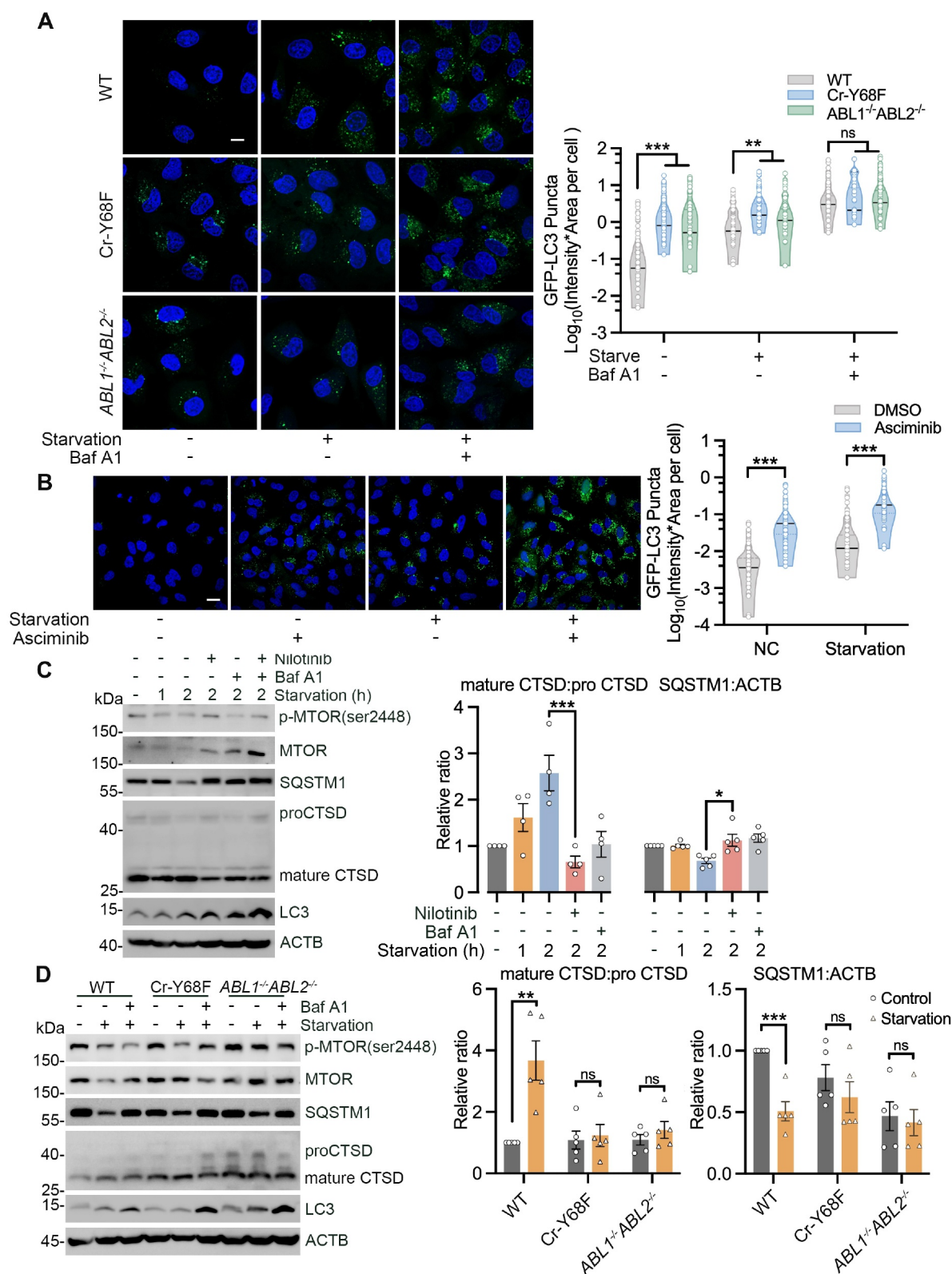
Figure 6. ABL1-mediated ATP6V1B2 Y68 phosphorylation regulates autophagy flux. (A and B) wild-type or mutated A549 cells subjected to the indicated treatments were stably transfected with a puromycin-inducible GFP-LC3 lentivirus at an MOI of 5. Autophagosomes levels were represented by the presence of GFP-LC3 in cells (A scale bar: 10 µm; B scale bar: 20 µm) (left panel). Plots show the quantification of the average intensity * area of GFP-LC3 puncta per cell, as analyzed by ImageJ (*n* = 50–95 cells, Student's t test for two groups, two-way ANOVA with Tukey's test for multi-groups and multiple tests (the horizon line indicated that the level of statistical significance between WT and Cr-Y68F cells is the same as that between WT and *ABL1⁻/⁻ABL2⁻/⁻* cells), right panel). (C and D) wild-type, mutated or knockout A549 cells subjected to the indicated treatments were analyzed by immunoblotting with antibodies against autophagy-associated proteins. The protein levels were quantitatively analyzed using ImageJ and are shown as box plots (*n* = 4 (C) or 5 (D), one-way ANOVA (C) or two-way ANOVA(D) with Tukey's test for multi-groups and multiple tests. All plots show the results from at least three independent biological replicates for each experimental condition (***$p < 0.001$, **$p < 0.01$ and *$p < 0.05$; ns, no significant difference).
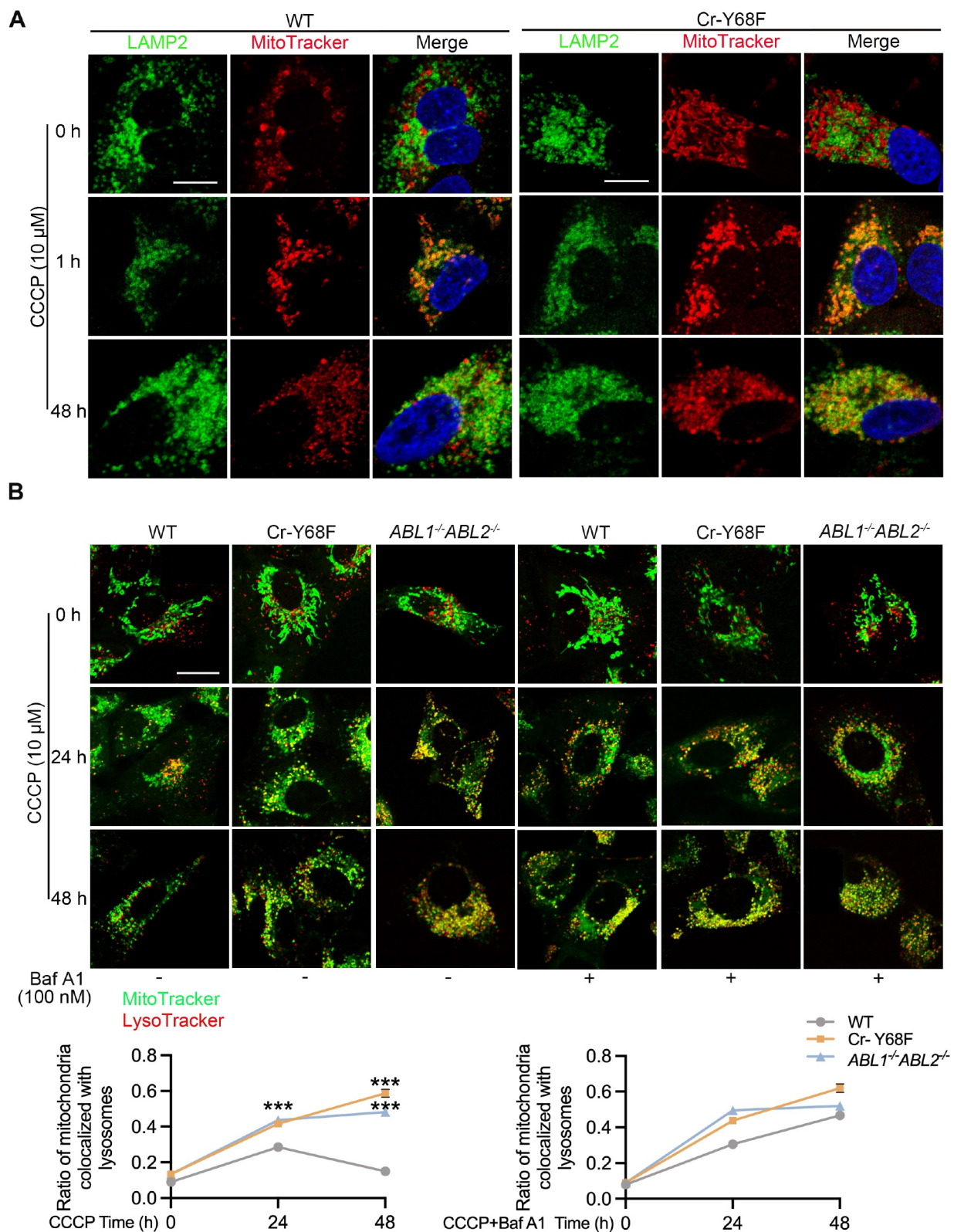
Figure 7. The phosphorylation of ATP6V1B2 at Y68 is involved in mitophagy. (A) fluorescence colocalization of mitochondria and lysosomes in A549 cells stained for LAMP2 and pyruvate dehydrogenase in the mitochondrial matrix upon 10 μM CCCP treatment for the indicated number of hours (scale bar: 10 μm). (B) living cells stained with MitoTracker (deep Red[FM], emission dispensable for the mitochondrial membrane potential) and LysoTracker were treated with 10 μM CCCP and subjected to real-time fluorescence microscopy (scale bar: 10 μm). The ratio of mitochondria colocalized with lysosomes was analyzed with ImageJ and Student's t test for each group compared with that of the WT group (each point = 5 randomly selected images, each of which contains at least 20 cells, two-way ANOVA with Tukey's test for multi-groups and multiple tests, ***$p < 0.001$). At least three independent replicates of all the experiments were performed.
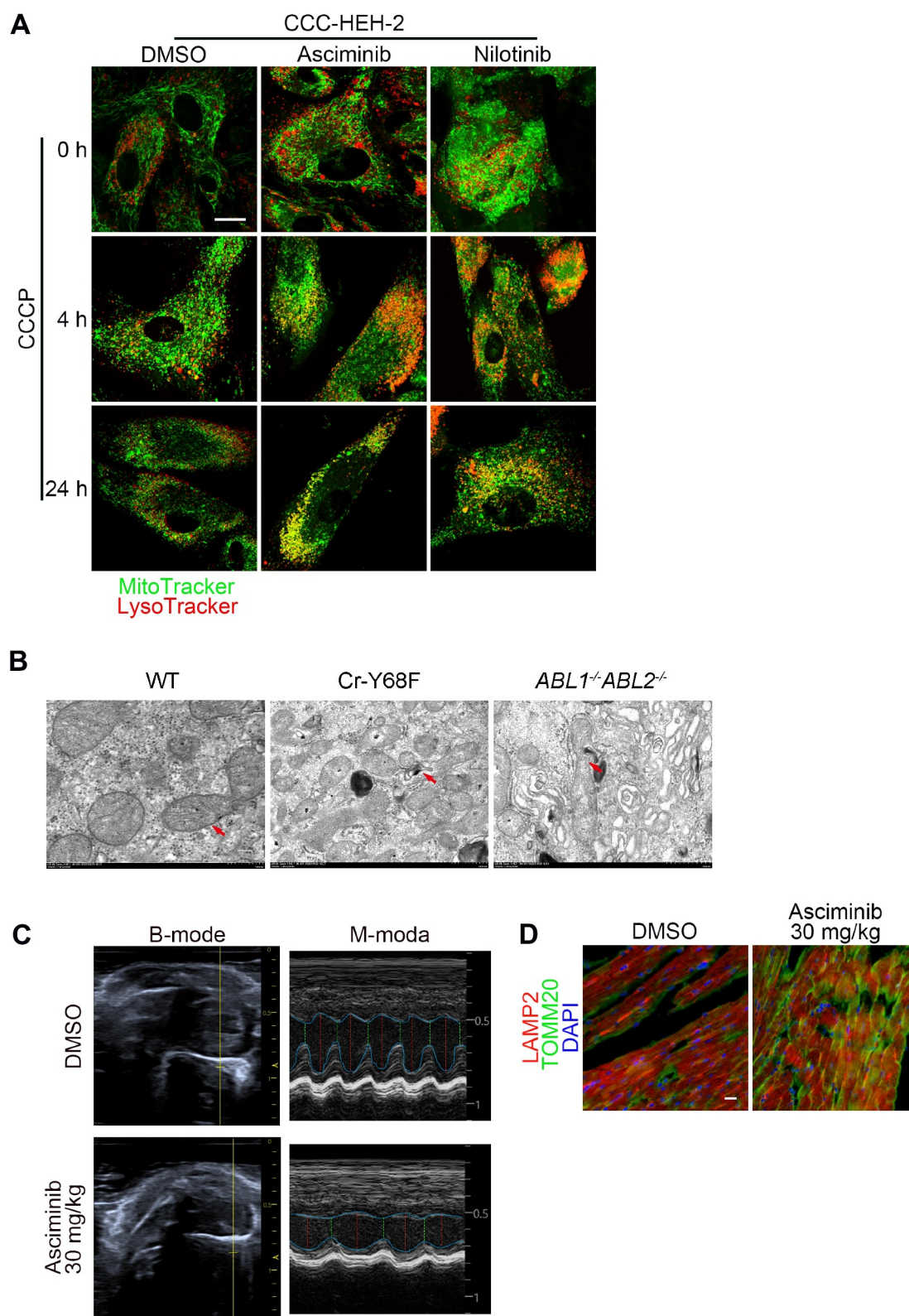
Figure 8. Inhibition of ABL1 activity is involved in mitophagy. (A) living CCC-HEH-2 cells pretreated with 10 μM asciminib or 5 μM nilotinib and then treated with CCCP (10 μM) and labeled with MitoTracker and LysoTracker, which were detected via immunofluorescence microscopy (scale bar: 10 μm). (B) TEM observations of mitochondria in starved cells (scale bar: 1 μm). (C) asciminib causes cardiac dysfunction in mice. C57BL/6J mice (*n* = 8) were treated with DMSO or 30 mg/kg asciminib for 6 weeks via oral gavage. The cardiac function of C57BL/6J mice was analyzed. (D) Representative images of cardiac sections stained with anti-LAMP2 and anti-TOMM20 antibodies (scale bar: 10 μm). All plots show the results from at least three independent biological replicates for each experimental condition.
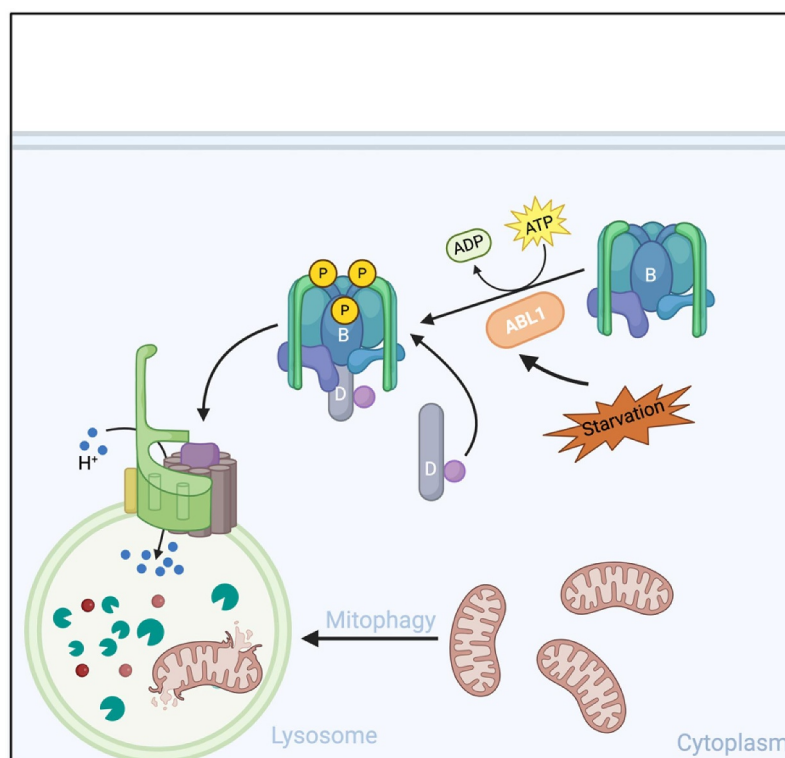
Figure 9. ABL1-mediated ATP6V1B2 phosphorylation facilitates V-ATPase assembly and lysosomal acidification. Schematic of the model of ABL1-regulated V-ATPase activity and lysosomal acidity. ATP6V1B2 (B) is phosphorylated by ABL1, which is potentiated upon amino acid starvation. Tyrosine phosphorylation of ATP6V1B2 facilitates the binding of ATP6V1B2 to ATP6V1D (D), thereby prompting the assembly of V_1 subcomplexes and, in turn, the full complexes of V-ATPase in the lysosome. ABL1-dependent lysosome acidification is indispensable for lysosomal digestion in the processes of autophagy and mitophagy (created in BioRender.com).

ABL1 phosphorylates a panel of substrates in response to cellular stress [54]. The activity of ABL1 was increased under starvation conditions (Figure S1A), and the ABL1-ATP6V1B2 interaction and ATP6V1B2 phosphorylation level were increased (Figure 1E), suggesting that ABL1 may phosphorylate ATP6V1B2, and ABL1 directly mediated ATP6V1B2 phosphorylation ATP6V1B2 in vitro (Figure 3C), which supports our hypothesis. ABL1 contains an SH3 domain that interacts with the PXXP motif in the substrate for substrate recognition and an SH2 domain that interacts with a phosphorylated tyrosine. In this work, ATP6V1B2 expressed in the presence of ABL1 interacted with ABL1 SH2 but not SH3, as shown by the GST-ABL1 SH3 pull-down assay (Figure 2A) and far western blot (Figure 2B). Consistent with this finding, the inhibition of ATP6V1B2 phosphorylation essentially disrupted the interaction of ATP6V1B2 with the SH2 domain (Figure 2B). In addition, lower levels of phosphorylated ATP6V1B2 were observed in cells expressing ATP6V1B2^{Y68F} (Figures 3I and 4E), which indicated that ATP6V1B2 May have other phosphorylation sites that are not phosphorylated ABL1 (Figures 3G–3I and S2D). These results suggest that the phosphorylation of ATP6V1B2 contributes to the binding of the ABL1-SH2 domain to ATP6V1B2, which subsequently facilitates the further phosphorylation of ATP6V1B2, and this phosphorylation enhances the ABL1-ATP6V1B2 interaction, and thus results in a cascade effect. Whereas ATP6V1B2(Δ1–49) and ATP6V1B2^{P15,18A}, both disrupted PXXP motif for SH3 domain binding, were failed to interact with ABL1 and

showed significantly attenuated phosphorylation (Figure 2E). These results suggested that the SH3 domain, together with other motif in ABL1, are responsible for the substrate recognition and contribute to the initial phosphorylation. This finding was also supported by the finding that ATP6V1B2 exhibited a weak associated with and was nearly not phosphorylated by ABL2, which shares ~ 90% homology in the SH3 domain with ABL1. These findings support a model in which ABL1 interacts with ATP6V1B2 and initiates tyrosine phosphorylation, which in turn reinforces the interactions via the SH2 domain, resulting in much higher phosphorylation levels, as observed in other phosphorylated substrates of ABL1 [55].

The depletion of *ABL1* and *ABL2* simultaneously causes early embryonic lethality, and the single knockout of *ABL2* causes normal development but abnormal behaviors in mice [56], which suggests that ABL1 and ABL2 have overlapping roles but that ABL1 also has indispensable functions. Autophagy is needed for multiple functions during embryogenesis [57]. ATP6V1B2, a proton pump subunit that is phosphorylated by ABL1 but poorly phosphorylated by ABL2, suggests that ABL1 May have functions that cannot be replaced by ABL2 during development. Differential binding to ATP6V1B2 and the regulation of V-ATPase may represent a mechanism that explains the different functions of ABL1 and ABL2.

ABL1 is activated by several stress stimuli, including ionizing irradiation, oxidative stress and starvation [54,58], which are associated with autophagy. In this study, both amino acid

starvation and serum starvation induced the ABL1-ATP6V1B2 interaction and ATP6V1B2 phosphorylation (Figure 1E). The incorporation of cytosolic ATP6V1B2 into lysosomes under amino acid starvation depended on the phosphorylation of ATP6V1B2 by ABL1 (Figures 4A and S3A) and was independent of MTORC1 signaling (Figure 6C), suggesting that we may have identified an important new mechanism for controlling V-ATPase assembly.

ABL1 promotes V-ATPase assembly by phosphorylating ATP6V1B2 under starvation conditions, and cells treated with nilotinib or asciminib presented hypoacidified and dyspeptic lysosomes (Figures 5F and S4C). These results suggest that ABL1 may participate in lysosome-related biological processes and diseases. Under starvation, the abundant autophagic cargo needs more acidified mature lysosomes, and ABL1 deficiency may result in the hypo-acidification of lysosomes and impede the final digestion of the molecules in autolysosomes. In contrast, abnormally activated ABL1 may resulted in the hyperacidification of lysosome and has been shown to play an important role in neurodegenerative diseases, especially Alzheimer disease and PD [59]. Activated ABL1 phosphorylates PHB2 to aggravate mitophagy disorder in a PD model [60,61], and the inhibition of ABL1 activation has been reported to restore the NPA model by activating the damaged autophagy pathway [31,62]. Similar findings were observed with TMEM175, which is involved in the pathogenesis of PD by preventing lysosomal hyperacidification and contributes to maintaining lysosomal pH [63].

ABL kinase inhibitors such as imatinib and dasatinib are the first-line therapeutics for CML and metastatic gastrointestinal stromal tumors [50,64], and severe cardiotoxicity has been observed in imatinib-treated patients. Imatinib is associated with impaired mitochondria [65,66]. Our results revealed that, upon the administration of the ABL1 inhibitor, mitochondria translocated into lysosomes (Figure S6A), which were hypoacidified and dyspeptic (Figures 5F and 6B), suggesting that mitochondrial dysfunction occurred when the cells were exposed to a high dosage of nilotinib. The Analyses of the biopsies from treated patients and mice exhibits mitochondrial abnormalities in the cardiomyocytes, and the investigations of isolated cardiomyocytes suggest that mitochondria were a primary target of imatinib [50,65]. Our results also revealed that the lysosomal accumulation of damaged mitochondria was induced by CCCP, and that damaged mitochondria accumulated in lysosomes via mitophagy but were not efficiently eliminated in damaged lysosomes after treatment with ABL1 inhibitors (Figure 8A). Furthermore, asciminib-treated mice presented cardiac dysfunction, and cardiac sections revealed the significant colocalization of mitochondria and lysosomes (Figure 8C, D). Taken together, our results provide a possible mechanistic explanation for the cardiotoxicity of ABL kinase inhibitors. Considering the vital role of lysosomal acidification in cells, this work may be important for understanding the vital roles of ABL1 in biological processes and diseases.

Materials and methods

Plasmids and generation of ATP6V1B2 mutants

MYC-tagged vectors for ABL1 and $ABL1^{K290R}$ expression were constructed by cloning the ABL1 gene into the pCMV-Myc vector (Clontech 635,689). The ATP6V1B2-Flag expression plasmid was obtained from Origene (RC205447), and the Flag-tagged ATP6V1B2 deletion mutants were generated by cloning the gene fragment amplified by polymerase chain reaction into the Flag vector. Flag-tagged ATP6V1B2 mutants of the nucleotide encoding a specific amino acid were constructed using a QuickMutation™ Site-Directed Mutagenesis Kit (Beyotime, D0206) with the following primers: i) 5'-ACGGGGCCGCAGCCGAGCTAGCCGTGCC-3' for the $ATP6V1B2^{P15,18A}$ mutant, ii) 5'-GTTAAGTT TCCCAGGTTTGCTGAAATTGTCCA-3' for the ATP6V1 $B2^{Y68F}$ mutant, iii) 5'-GATTTAGCCACGATATTTGAACG CGCTGGGCGA-3' for the $ATP6V1B2^{Y326F}$ mutant, and iv) 5'-GATGTATCTAACCAGCTATTTGCGTGCTATGCTATT GGA-3' for the $ATP6V1B2^{Y423F}$ mutant. GST fusion proteins were generated by cloning in pGEX4T-t-1 vectors (Amersham Biosciences Biotech Inc.) and expression in E. coli BL21 (DE3). The authenticity of all the constructs was verified by DNA sequencing.

Mammalian cell lines and transfection

Human embryonic kidney (HEK) 293 cells (Cell Resource Center, HEK 293) and a human cervical carcinoma cell line (HeLa cells; Cell Resource Center, HeLa) were cultured in Dulbecco's modified Eagle's medium (DMEM; Gibco, C11995500BT) supplemented with 10% fetal bovine serum (ExCell, FSP500), 100 units/ml penicillin, and 100 μg/ml streptomycin. Wild-type, $ABL1^{-/-}$ $ABL2^{-/-}$ and ATP6V1B2 (Cr-Y68F) A549 strains and were grown in Ham's F-12K (Kaighn's) medium (F12-K; Gibco 21,127,022) containing the same before mentioned supplements. All the cells were grown at 37°C in an atmosphere with 5% CO_2. Transient transfections were performed with Lipofectamine 2000 (Invitrogen 11,668,019) or the TransIT-X2® Dynamic Delivery System (Mirus, MIR 6000). The cells were treated with nilotinib (Novartis, S0045), asciminib (MedChemExpress, HY-104010), and Baf A1 (bafilomycin A1; Millipore,19600) as described in the article.

Generation of ATP6V1B2 (cr-Y68F) and $ABL1^{-/-}$ $ABL2^{-/-}$ A549 cells

ATP6V1B2 (Cr-Y68F) cells, in which the A in the codon encoding Y68 of ATP6V1B2 was mutated to T resulted in the substitution of Y68 with F68 in the two chromosomes, and $ABL1^{-/-}$ $ABL2^{-/-}$ A549 cells which contain frameshifts in two chromosomes of ABL1 and ABL2 in A549 cells were generated using a CRISPR-Cas9 system [67]. The guide RNA (sgRNA) and donor (sgRNA-ABL1: 5´-TGTGATTA TAGCCTAAGACC-3´, sgRNA-ABL2: 5´-AGTTCGCTCTA AGAATGGGC-3´, sgRNA-ATP6V1B2(Cr-Y68F): 5'-ATGGA CAATTTCAGCATACC-3', and donor-ATP6V1B2(Cr-Y68F) : 5'-CGGATATTGATCCTTTATTTTTTTCTCTTTAGTTTCC CAGGTTTGCTGAAATTGTCCATTTGACCTTACCGGAT-GGCACAAAGA-3') were designed to generate $ABL1^{-/-}$ $ABL2^{-/-}$ and ATP6V1B2 (cr-Y68F) lines. The DNA

fragments encoding the sgRNAs were cloned and inserted into the pSpCas9 (BB)-2A-puro vector (Addgene 48,139; deposited by Qincai Dong), and the resulting plasmids were subsequently transfected into A549 cells (Cell Resource Center, A549) together using the TransIT-X2® Dynamic Delivery System (Mirus, MIR 6000). The cells were then screened with puromycin (MCE, HY-B1743A), and monoclonal cell lines were obtained by serial dilution. The frameshifts in the *ABL1* and *ABL2* genes, and the replacement of A with T which resulted in the replacement of Y68 with F in ATP6V1B2 were confirmed by PCR and DNA sequencing.

Immunoprecipitation and immunoblot analysis

The cells were lysed in lysis buffer (50 mm Tris-HCl, pH 7.5, 150 mm NaCl, 1 mm EDTA, 1 mm EGTA, 1% [v:v] Triton X-100 [Sigma-Aldrich, T8787], and 0.5% [v:v] Tween 20 [Sigma-Aldrich 655,206] or M-PER^{TM} Mammalian Protein Extraction Reagent [Thermo 78,501] supplemented with the complete protease inhibitor cocktail [Roche 04,693,132,001] and the phosphatase inhibitor cocktail [Roche 04,906,837,001]). The soluble protein was immunoprecipitated with anti-Flag (agarose-conjugated, *M*-2; Sigma-Aldrich, A2220), anti-ABL1 (8E9; Santa Cruz Biotechnology, sc -56,887), anti-ATP6V1B2 (C-9; Santa Cruz Biotechnology, SC-166122) or anti-mouse IgG Sepharose® Bead Conjugate; Cell Signaling Technology, 3420 antibodies. An aliquot of total lysate (5%, v:v) was included as a loading control. The immunoblot analysis was performed with HRP-conjugated anti-ABL1 (8E9; Santa Cruz Biotechnology, sc -56,887 hRP; 1:250 dilution), anti-ATP6V1B2 (Sigma-Aldrich, HPA00814; 1:1000 dilution), HRP-conjugated anti-ACTB/β-actin (Sigma-Aldrich, A3854; 1:5000 dilution), HRP-conjugated anti-Flag (Sigma-Aldrich, A8592; 1:2000 dilution), HRP-conjugated anti-MYC (Sigma-Aldrich, SAB4200742; 1:1000 dilution), HRP-conjugated anti-phosphotyrosine (4G10; Millipore, 16–105; 1:1000 dilution), HRP-conjugated anti-His (H-3; Sigma-Aldrich, sc-8036 hRP; 1:1000 dilution), HRP-conjugated anti-GST (Invitrogen, MA4–004-HRP; 1:1000 dilution), anti-phospho-ATP6V1B2(Y68) (custom synthesized by General Biol [Anhui] Co, Ltd.;1:2000 dilution), anti-ATP6V1D (Proteintech 14,920–1-AP; 1:1000 dilution), anti-ATP6V0D1 (Abcam, ab202899; 1:1000 dilution), anti-ATP6V1A (Invitrogen, MA5–27729; 1:1000 dilution), anti-CTSD/cathepsin D (R&D systems, AF1014; 1:1000 dilution), anti-phospho-MTOR (Ser2448; Proteintech 67,778–1-AP; 1:1000 dilution), anti-phospho-MTOR (Ser2448) (Proteintech 67,778–1-AP; 1:1000 dilution), anti-MTOR (Proteintech 28,273–1-AP; 1:1000 dilution), anti-SQSTM1/p62 (Gene Tex, GTX629890; 1:1000 dilution), HRP-conjugated anti-MAP1LC3 (G-2, Santa Cruz Biotechnology, sc -271,625 hRP, 1:1000 dilution) or anti-LAMP2 (H4B4, Santa Cruz Biotechnology, sc -18,822, 1:1000 dilution) antibodies. The antigen-antibody complexes were visualized via chemiluminescence (ECL; Millipore, WBKLS0500) with an Amersham Imager 600 (GE Healthcare) or Touch Imager^{TM} (e-Blot). Full-scan immunoblots can be accessed from the source data file.

In vitro binding assay

GST fusion proteins were purified from *E. coli* BL21 (DE3) extracts via affinity chromatography using glutathione Sepharose beads (GE Healthcare 17,075,601).

For the GST affinity-isolation assay, the cell lysates were incubated with 1 μg of GST, GST-ABL1-SH2 or GST-ABL1-SH3 immobilized on the beads for 2 h at 4°C. The adsorbates were washed with lysis buffer and then subjected to SDS-PAGE and immunoblot analysis. An aliquot of the total lysate (5%, v:v) was included as a loading control for SDS-PAGE.

For the far western binding assays, the immunoprecipitates were separated on SDS-PAGE gels and then transferred to PVDF membranes. The membranes were incubated with purified GST, GST-ABL1-SH2 and GST-ABL1-SH3 proteins at room temperature for 2 h. The binding between the GST fusion proteins and the PVDF membrane was analyzed by immunoblotting using an anti-GST antibody.

Immunofluorescence staining and microscopy

The cells were treated, fixed, permeabilized, and blocked as previously described. After an incubation with anti-LAMP2 (1:200 dilution) and/or anti-ATP6V1B2 (1:100 dilution) antibodies at 4°C overnight, the cells were washed three times with PBS (Gibco 10,010,023) and then incubated with FITC- or TRITC-conjugated goat anti-rabbit (or anti-mouse) IgG (ZSGB-Bio, ZF-0311, ZF-0312, ZF-0316, ZF-0313) for 1 h at room temperature. Next, after washing, the cells were stained with DAPI using Mounting Medium with DAPI-Aqueous Fluoroshield (Abcam, ab104139) and imaged using a laser scanning confocal microscope (Zeiss LSM 800 Meta, built-in software ZEN2.3) with a 63× oil immersion lens.

In situ proximity ligation assay

The Duolink *in situ* proximity ligation assay (Sigma-Aldrich, DUO92008) enables the endogenous detection of protein interactions and posttranslational modifications of proteins at the single-molecule level in fixed cell and tissue samples. Briefly, A549 cells plated on glass coverslips were fixed with 4% formaldehyde, and the cells were permeabilized with 0.2% Triton X-100 in PBS for 15 min. After blocking with Duolink Blocking Solution(Sigma-Aldrich, DUO82007), the cells were incubated with rabbit anti-ATP6V1B2 (Sigma-Aldrich, HPA00814, 1:100 dilution) and mouse anti-ABL1 (8E9, Santa Cruz Biotechnology, sc -56,887, 1:50 dilution) or mouse anti-phosphotyrosine (4G10, Millipore, 05–321, 1:100 dilution) or mouse anti-ATP6V0D1 (Abcam, ab56441, 1:100 dilution) primary antibodies and then incubated with oligonucleotide-labeled anti-mouse IgG (Sigma-Aldrich, DUO92004) and anti-rabbit IgG (Sigma-Aldrich, DUO92002) according to the manufacturer's instructions for PLA. Anti-ATP6V1B2 or anti-ABL1alone was used as a negative control. The red fluorescent spots generated from the DNA amplification-based reporter system, which indicate that the two primary antibodies are in sufficiently close proximity, were detected with an LSM 800 Meta confocal microscope (Zeiss).

LC-MS/MS analysis

Anti-Flag immunoprecipitates prepared from lysates of HEK293 cells transfected with MYC-ABL1 and Flag-ATP6V0D1 or ATP6V1B2-Flag were resolved by SDS-PAGE, after which the protein bands were excised and subjected to trypsin digestion. LC-electrospray ionization-MS/MS-resolved peptides were analyzed using a Q-TOF2 system (Micromass), and the data were compared against the SwissProt database using the Mascot search engine (http://www.matrixscience.com) for phosphorylation.

In vitro tyrosine kinase assay

Purified recombinant GST-ATP6V1B2 (0.5 μg) or GST-CRK was incubated with active, recombinant ABL1 (0.02 μg, Millipore, 14–529) in kinase reaction buffer (20 mm HEPES, pH 7.0, 75 mm KCl, 10 mm $MgCl_2$, and 10 mm $MnCl_2$) plus 2 mm ATP (Sigma-Aldrich, A6559) for 30 min at 37°C. The reaction products were analyzed by SDS-PAGE and immunoblotting with an anti-p-Tyr antibody.

In vitro binding of ATP6V1B2 and ATP6V1D

In vitro binding of ATP6V1B2 and ATP6V1D was performed according to a previous report [68,69]. First, whole-cell extracts of the cells coexpressing MYC-ABL1 and ATP6V1B2-Flag or ATP6V1B2(Y68F)-Flag were prepared by using lysis buffer containing complete protease inhibitor cocktail and phosphatase inhibitor cocktail on ice for 20 min, and then centrifuged at 14,000×g for 10 min. Afterward, the supernatants were treated with/without 2 μL of alkaline phosphatase (Sigma-Aldrich, P0114) at 37°C for 1 h, and the lysates were subjected to immunoprecipitation with anti-Flag beads at 4°C for 2 h. Next, after being washed three times with lysis buffer, the immunoprecipitates were resuspended in 200 μL of lysis buffer containing Flag peptides at final concentration of 100 nM (Sigma-Aldrich, F3290) and incubated at 4°C for 1 h, and then filtered via the Pierce™ Protein Concentrator PES (30K MWCO; Milipore 88,502). Flag-tagged proteins were diluted (1:3 v:v) with low-salt buffer, and then 2 μg of His-tagged recombinant human ATP6V1D protein (Solarbio, P03212) was added. Finally, the mixture containing purified ATP6V1B2-Flag and His-V1D was subjected to immunoprecipitation with anti-Flag-conjugated beads at 4°C for 2 h. After three washes, the immunoprecipitates were analyzed by SDS-PAGE and immunoblotting.

Lysosome isolation and lysosomal V-ATPase activity assay

Lysosomes were isolated using a lysosomal extraction kit (Solarbio, EX2670). Briefly, cells were washed three times with PBS, and then, 400 μL of cold reagent A was added and incubated at 4°C for 10 min. Next, the cell suspension was homogenized with a Dounce homogenizer 30–40 times, and the homogenates were centrifuged at 1000×g for 5 min at 4°C. Next, the supernatant was sequentially centrifuged at 3000×g and 5000×g for 10 min, after which the pellet was removed, and the supernatant was collected. Subsequently, the supernatant was centrifuged at 25,000×g for 20 min, and the pellet was collected and suspended in 400 μL of cold Reagent B. Finally, the supernatant was centrifuged at 25,000×g for 20 min at 4°C, and the precipitate was collected and then resuspended in 100 μL of lysosome preservation solution C for subsequent experiments.

An ATPase/GTPase activity assay kit (Sigma-Aldrich, MAK113) was used to determine the V-ATPase activity. Five microliters of the lysosomal preparation, which was normalized based on the ATP6V0D1 level detected by immunoblotting, was mixed with 15 μL of assay buffer in a 96-well plate. The reaction was started by adding 10 μL of 4 mm ATP, and the samples were incubated for 30 min at room temperature. Then, 200 μL of REAGENT (MAK113A) was added to each well, and the samples were incubated for another 30 min at room temperature to terminate the enzyme reaction and generate the colorimetric product. The plates were read at OD620 nm in a Multiskan SkyHigh (Thermo, A51119500C), and the amount of ATP hydrolyzed was calculated form a standard curve.

Lysosomal pH measurement

The lysosomal pH was measured with a pH-sensitive dye (fluorescein isothiocyanate) conjugated with dextran-10 kD (FITC-Dextran; Sigma-Aldrich, FD10S) and a pH-insensitive dye (tetramethylrhodamine) conjugated with dextran-10 kD (TMR-Dextran; Invitrogen, D1868) as reference [39]. Briefly, cells seeded in 6-well plates were loaded with 0.5 mg/mL FITC-dextran and TMR-dextran (final concentration) overnight and chased in medium without dye for three hours before analysis. The cells were washed with Live Cell Imaging Solution (Invitrogen, A14291DJ) and scanned using a high-content screening system (PerkinElmer, Opera Phenix). The fluorescence emission was recorded at 520 nm and 580 nm after excitation at 488 nm and 550 nm, respectively, and the fluorescence intensity ratio (Fluorescein at 520 nm/580 nm) was calculated with Harmony version 4.9. Standard buffers were prepared at various pH values ranging from 4.5 to 7.5 and supplemented with 10 mm valinomycin and 10 mm nigericin (Intracellular pH Calibration Buffer Kit; Invitrogen, P35379). The ratio of fluorescence at 520 and 580 nm in response to various pH values was fitted to a linear equation to generate a pH standard curve. The lysosomal pH values were then calculated from the resulting intensity ratio (520 nm/580 nm) based on the standard curve.

The lysosomal lumenal pH was also measured with a fluorescein isothiocyanate (FITC)-dextran probe together with a dual-emission ratiometric technique. FITC shows a pH-dependent variation in fluorescence when analyzed at maximum emission wavelength (610 nm) and no variation when analyzed at the isosbestic point (515 nm), therefore, the ratio can be used to determine the lysosomal pH.

LysoTracker and MitoTracker staining

For an approximate assessment of lysosomal acidity, the cells were cultured in a 6-well dish or 6-mm dish one day before the experiment. Acidic organelles were visualized by adding

50 nM (final concentration) LysoTracker Red DND-99 (Invitrogen, L7528) or an appropriate amount of CellLight® Lysosomes-GFP (BacMam 2.0; Invitrogen, C10507; specific for LAMP2 in the lysosomal membrane) to the cell culture medium, and the cells were incubated at 37°C for 45 min or overnight. The cells were then washed twice with PBS and maintained in Live Cell Imaging Solution (Invitrogen, A14291DJ) for imaging or in PBS for flow cytometry analysis. Images were acquired using a Zeiss LSM 800 Meta fluorescence microscope, and the fluorescence intensity of LysoTracker was obtained with a BD Biosciences FACSCalibur instrument.

For mitochondrial visualization, 100 nM (final concentration) MitoTracker™ Deep Red FM (Invitrogen, M22426; for staining of live mitochondria) or an appropriate amount of CellLight® Mitochondria-GFP (BacMam 2.0) (Invitrogen, C10600; specific for pyruvate dehydrogenase in the mitochondrial matrix) was added to the cell culture medium and incubated at 37°C for 45 min or overnight. The fluorescence emission (665 nm) was acquired after excitation at 644 nm with a fluorescence microscope.

Lysosomal hydrolytic activity assay

The activities of CTSD and CTSB in lysosomes were determined using Pepstatin A BODIPYTM FL (Invitrogen, P12271) for CTSD and Magic Red Cathepsin B assay kits (ImmunoChemistry Technologies, 937) for CTSB. Pepstatin A BODIPYTM FL and Magic Red stock solutions were prepared according to the manufacturer's instructions. The cells were incubated with Magic Red (1:1,000 dilution) or Pepstatin A BODIPY FL (2 mm) at 37°C for 1 h, washed twice with PBS, and then subjected to imaging with a confocal microscope or flow cytometry analysis.

Transmission electron microscopy (TEM)

After starvation, the cells were washed with PBS, fixed with 2.5% glutaraldehyde, and then prestained with osmium tetroxide. Eighty-nanometer-thick serial sections were then cut and stained with uranyl acetate and lead citrate. Images were acquired with a transmission electron microscope (Hitachi, H-7650) operating at 80 kV.

Quantification and statistical analysis

The intensities of the immunoblotted bands were measured using FiJi (ImageJ software). The statistical analysis was performed using GraphPad Prism 9.0 software. At least three independent experiments were performed to generate each dataset. The data are presented as the means ± SEMs (standard errors of the means). When box plots are presented, the box represents the 5%-95% range or the full range, with the solid line within them indicating the mean level and points outside indicating data in the 0%-5% and 95%-100% ranges, alternatively, all points are shown as individual data. When violin plots are presented, the violin represents the distribution of data, with the solid line within the violin indicating the mean level and the dashed line indicating the concentration of

the data. Statistical significance was calculated using Student's t test for two groups and by one-way ANOVA or two-way ANOVA with Tukey's test for multiple groups. *, ** and *** indicate $p < 0.05$, $p < 0.01$ and $p < 0.001$, respectively, ns indicates no significance.

Disclosure statement

No potential conflict of interest was reported by the author(s).

Funding

References

[1] Mindell JA. Lysosomal acidification mechanisms. Annu Rev Physiol. 2012;74(1):69–86. doi: 10.1146/annurev-physiol-012110-142317
[2] Ohkuma S, Moriyama Y, Takano T. Identification and characterization of a proton pump on lysosomes by fluorescein-isothiocyanate-dextran fluorescence. Proc Natl Acad Sci USA. 1982;79(9):2758–2762. doi: 10.1073/pnas.79.9.2758
[3] Kissing S, Saftig P, Haas A. Vacuolar ATPase in Phago(Lyso)Some biology. Int J Med Microbiol. 2018;308(1):58–67. doi: 10.1016/j.ijmm.2017.08.007
[4] Pamarthy S, Kulshrestha A, Katara GK, et al. The curious case of vacuolar ATPase: regulation of signaling pathways. Mol Cancer. 2018;17(1):41. doi: 10.1186/s12943-018-0811-3
[5] Colacurcio DJ, Nixon RA. Disorders of lysosomal acidification—the emerging role of v-ATPase in aging and neurodegenerative disease. Ageing Res Rev. 2016;32:75–88. doi: 10.1016/j.arr.2016.05.004
[6] Gruenberg J, van der Goot FG. Mechanisms of pathogen entry through the endosomal compartments. Nat Rev Mol Cell Biol. 2006;7(7):495–504. doi: 10.1038/nrm1959
[7] Toei M, Saum R, Forgac M. Regulation and isoform function of the V-ATPases. Biochemistry. 2010;49(23):4715–4723. doi: 10.1021/bi100397s
[8] Zhao J, Benlekbir S, Rubinstein JL. Electron cryomicroscopy observation of rotational states in a Eukaryotic V-ATPase. Nature. 2015;521(7551):241–245. doi: 10.1038/nature14365
[9] Abbas YM, Wu D, Bueler SA, et al. Structure of V-ATPase from the mammalian brain. Science. 2020;367(6483):1240–1246. doi: 10.1126/science.aaz2924
[10] Mazhab-Jafari MT, Rohou A, Schmidt C, et al. Atomic model for the membrane-embedded VO motor of a Eukaryotic V-ATPase. Nature. 2016;539(7627):118–122. doi: 10.1038/nature19828
[11] Kane PM. Regulation of V-ATPases by reversible disassembly. FEBS Lett. 2000;469(2–3):137–141. doi: 10.1016/S0014-5793(00)01265-5
[12] M Kane P. Targeting reversible disassembly as a mechanism of controlling V-ATPase activity. CPPS. 2012;13(2):117–123. doi: 10.2174/138920312800493142
[13] Collins MP, Forgac M. Regulation and function of V-ATPases in physiology and disease. Biochim et Biophys Acta (BBA) - Biomembr. 2020;1862(12):183341. doi: 10.1016/j.bbamem.2020.183341
[14] Su Y, Zhou A, Al-Lamki RS, et al. The A-Subunit of the V-Type H±ATPase interacts with phosphofructokinase-1 in humans. J Biol Chem. 2003;278(22):20013–20018. doi: 10.1074/jbc.M210077200
[15] Nakamura S. Glucose activates H⁺-ATPase in kidney epithelial cells. Am J Physiol-Cell Physiol. 2004;287(1):C97–C105. doi: 10.1152/ajpcell.00469.2003

[16] Sautin YY, Lu M, Gaugler A, et al. Phosphatidylinositol 3-kinase-mediated effects of glucose on vacuolar H $^+$ -ATPase assembly, translocation, and acidification of intracellular compartments in renal epithelial cells. Mol Cell Biol. 2005;25(2):575–589. doi: 10.1128/MCB.25.2.575-589.2005

[17] Stransky LA, Forgac M. Amino acid availability modulates vacuolar H+-ATPase assembly. J Biol Chem. 2015;290(45):27360–27369. doi: 10.1074/jbc.M115.659128

[18] Jewell JL, Russell RC, Guan K-L. Amino acid signalling upstream of mTOR. Nat Rev Mol Cell Biol. 2013;14(3):133–139. doi: 10.1038/nrm3522

[19] Nixon RA. The aging lysosome: an essential catalyst for late-onset neurodegenerative diseases. Biochim Et Biophys Acta (BBA) - Proteins Proteomics. 2020;1868(9):140443. doi: 10.1016/j.bbapap.2020.140443

[20] Yamamoto A, Yue Z. Autophagy and its normal and pathogenic states in the brain. Annu Rev Neurosci. 2014;37(1):55–78. doi: 10.1146/annurev-neuro-071013-014149

[21] Wang C, Telpoukhovskaia MA, Bahr BA, et al. Endo-lysosomal dysfunction: a converging mechanism in neurodegenerative diseases. Curr Opin Neurobiol. 2018;48:52–58. doi: 10.1016/j.conb.2017.09.005

[22] Nguyen DKH, Thombre R, Wang J. Autophagy as a common pathway in amyotrophic lateral sclerosis. Neurosci Lett. 2019;697:34–48. doi: 10.1016/j.neulet.2018.04.006

[23] Gatica D, Lahiri V, Klionsky DJ. Cargo recognition and degradation by selective autophagy. Nat Cell Biol. 2018;20(3):233–242. doi: 10.1038/s41556-018-0037-z

[24] Gyparaki M-T, Papavassiliou AG. Lysosome: the cell's 'suicidal bag' as a promising cancer target. Trends Mol Med. 2014;20(5):239–241. doi: 10.1016/j.molmed.2014.01.009

[25] de Duve C. The lysosome turns fifty. Nat Cell Biol. 2005;7(9):847–849. doi: 10.1038/ncb0905-847

[26] Levine B, Kroemer G. Biological functions of autophagy genes: a disease perspective. Cell. 2019;176(1–2):11–42. doi: 10.1016/j.cell.2018.09.048

[27] Galluzzi L, Baehrecke EH, Ballabio A, et al. Molecular definitions of autophagy and related processes. Embo J. 2017;36(13):1811–1836. doi: 10.15252/embj.201796697

[28] Galluzzi L, Green DR. Autophagy-independent functions of the autophagy machinery. Cell. 2019;177(7):1682–1699. doi: 10.1016/j.cell.2019.05.026

[29] Kawai A, Uchiyama H, Takano S, et al. Autophagosome-lysosome fusion depends on the pH in acidic compartments in CHO cells. Autophagy. 2007;3(2):154–157. doi: 10.4161/auto.3634

[30] Mauvezin C, Nagy P, Juhász G, et al. Autophagosome–lysosome fusion is Independent of V-ATPase-mediated acidification. Nat Commun. 2015;6(1):7007. doi: 10.1038/ncomms8007

[31] Marín T, Dulcey AE, Campos F, et al. C-Abl activation linked to autophagy-lysosomal dysfunction contributes to neurological impairment in Niemann-pick type a disease. Front Cell Dev Biol. 2022;10:844297. doi: 10.3389/fcell.2022.844297

[32] Karim MR, Liao EE, Kim J, et al. α-Synucleinopathy associated c-abl activation causes P53-dependent autophagy impairment. Mol Neurodegener. 2020;15(1):27. doi: 10.1186/s13024-020-00364-w

[33] Yogalingam G, Pendergast AM. Abl kinases regulate autophagy by promoting the trafficking and function of lysosomal components. J Biol Chem. 2008;283(51):35941–35953. doi: 10.1074/jbc.M804543200

[34] Bellodi C, Lidonnici MR, Hamilton A, et al. Targeting autophagy potentiates tyrosine kinase inhibitor–induced cell death in Philadelphia chromosome–positive cells, including primary CML stem cells. J Clin Invest. 2009;119(5):1109–1123. doi: 10.1172/JCI35660

[35] La Barbera L, Vedele F, Nobili A, et al. Nilotinib restores memory function by preventing dopaminergic neuron degeneration in a mouse model of Alzheimer's disease. Prog Neurobiol. 2021;202:102031. doi: 10.1016/j.pneurobio.2021.102031

[36] McGuire CM, Forgac M. Glucose starvation increases V-ATPase assembly and activity in mammalian cells through AMP kinase and phosphatidylinositide 3-Kinase/Akt signaling. J Biol Chem. 2018;293(23):9113–9123. doi: 10.1074/jbc.RA117.001327

[37] Cotter K, Stransky L, McGuire C, et al. Recent insights into the structure, regulation, and function of the V-ATPases. Trends Biochem Sci. 2015;40(10):611–622. doi: 10.1016/j.tibs.2015.08.005

[38] Forgac M. Vacuolar ATPases: rotary proton pumps in physiology and pathophysiology. Nat Rev Mol Cell Biol. 2007;8(11):917–929. doi: 10.1038/nrm2272

[39] Liu B, Palmfeldt J, Lin L, et al. STAT3 associates with vacuolar H ±ATPase and regulates cytosolic and Lysosomal pH. Cell Res. 2018;28(10):996–1012. doi: 10.1038/s41422-018-0080-0

[40] Yoshida A, Ohta M, Kuwahara K, et al. Purification and characterization of cathepsin B from the muscle of horse mackerel trachurus japonicus. Mar Drugs. 2015;13(11):6550–6565. doi: 10.3390/md13116550

[41] Creasy BM, Hartmann CB, White FKH, et al. New assay using fluorogenic substrates and immunofluorescence staining to measure cysteine cathepsin activity in live cell subpopulations. Cytometry. 2007;71A(2):114–123. doi: 10.1002/cyto.a.20365

[42] Lee J-H, Yu WH, Kumar A, et al. Lysosomal proteolysis and autophagy require presenilin 1 and are disrupted by alzheimer-related PS1 mutations. Cell. 2010;141(7):1146–1158. doi: 10.1016/j.cell.2010.05.008

[43] Wang R, Wang J, Hassan A, et al. Molecular basis of V-ATPase inhibition by Bafilomycin A1. Nat Commun. 2021;12(1):1782. doi: 10.1038/s41467-021-22111-5

[44] Martinez A, Lamaizon CM, Valls C, et al. C-Abl phosphorylates MFN2 to regulate mitochondrial morphology in cells under endoplasmic reticulum and oxidative stress, impacting cell survival and neurodegeneration. Antioxidants. 2023;12(11):2007. doi: 10.3390/antiox12112007

[45] Zhou L, Zhang Q, Zhang P, et al. C-Abl-mediated Drp1 phosphorylation promotes oxidative stress-induced mitochondrial fragmentation and neuronal cell death. Cell Death Dis. 2017;8(10):e3117–e3117. doi: 10.1038/cddis.2017.524

[46] Yang Q, Zhang C, Wei H, et al. Caspase-independent pathway is related to nilotinib cytotoxicity in cultured cardiomyocytes. Cell Physiol Biochem. 2017;42(6):2182–2193. doi: 10.1159/000479993

[47] Damrongwatanasuk R, Fradley MG. Cardiovascular complications of targeted therapies for chronic myeloid leukemia. Curr Treat Options Cardio Med. 2017;19(4):24. doi: 10.1007/s11936-017-0524-8

[48] Atallah E. Nilotinib cardiac toxicity: should we still Be concerned? Leuk Res. 2011;35(5):577–578. doi: 10.1016/j.leukres.2011.01.021

[49] Soutar MPM, Kempthorne L, Annuario E, et al. FBS/BSA media concentration determines CCCP's ability to depolarize mitochondria and activate PINK1-PRKN mitophagy. Autophagy. 2019;15(11):2002–2011. doi: 10.1080/15548627.2019.1603549

[50] Kerkelä R, Grazette L, Yacobi R, et al. Cardiotoxicity of the cancer therapeutic agent imatinib mesylate. Nat Med. 2006;12(8):908–916. doi: 10.1038/nm1446

[51] Tang Q, Liu M, Liu Y, et al. NDST3 Deacetylates A-tubulin and suppresses V-ATPase assembly and lysosomal acidification. Embo J. 2021;40(19):e107204. doi: 10.15252/embj.2020107204

[52] Gutiérrez-Pérez P, Santillán EM, Lendl T, et al. miR-1 sustains muscle physiology by controlling V-ATPase complex assembly. Sci Adv. 2021;7(42):eabh1434. doi: 10.1126/sciadv.abh1434

[53] Ratto E, Chowdhury SR, Siefert NS, et al. Direct control of lysosomal catabolic activity by mTORC1 through regulation of V-ATPase assembly. Nat Commun. 2022;13(1):4848. doi: 10.1038/s41467-022-32515-6

[54] Colicelli J. ABL tyrosine kinases: evolution of function, regulation, and specificity. Sci Signal. 2010;3(139). doi: 10.1126/scisignal.3139re6

[55] Liu X, Huang W, Li C, et al. Interaction between C-Abl and arg tyrosine kinases and proteasome subunit PSMA7 regulates proteasome degradation. Mol Cell. 2006;22(3):317–327. doi: 10.1016/j.molcel.2006.04.007

[56] Koleske AJ, Gifford AM, Scott ML, et al. Essential roles for the abl and arg tyrosine kinases in Neurulation. Neuron. 1998;21 (6):1259–1272. doi: 10.1016/S0896-6273(00)80646-7

[57] Allen EA, Baehrecke EH. Autophagy in animal development. Cell Death Differ. 2020;27(3):903–918. doi: 10.1038/s41418-020-0497-0

[58] Matsubara T, Ikeda M, Kiso Y, et al. C-Abl tyrosine kinase regulates serum-induced nuclear export of diacylglycerol kinase α by phosphorylation at tyr-218. J Biol Chem. 2012;287 (8):5507–5517. doi: 10.1074/jbc.M111.296897

[59] Feng L, Fu S, Yao Y, et al. Roles for C-Abl in postoperative neurodegeneration. Int J Med Sci. 2022;19(12):1753–1761. doi: 10.7150/ijms.73740

[60] Brahmachari S, Ge P, Lee SH, et al. Activation of tyrosine kinase C-Abl contributes to α-Synuclein–Induced neurodegeneration. J Clin Invest. 2016;126(8):2970–2988. doi: 10.1172/JCI85456

[61] Zhang Y, Wu J, Jin W, et al. Nonreceptor tyrosine kinase C-Abl-mediated PHB2 phosphorylation aggravates mitophagy disorder in Parkinson's disease model. Oxid Med Cell Longev. 2022;2022:1–13. doi: 10.1155/2022/8704016

[62] Contreras PS, Tapia PJ, González-Hódar L, et al. C-Abl inhibition activates TFEB and Promotes cellular clearance in a lysosomal disorder. iScience. 2020;23(11):101691. doi: 10.1016/j.isci.2020.101691

[63] Hu M, Li P, Wang C, et al. Parkinson's disease-risk protein TMEM175 is a proton-activated proton channel in lysosomes. Cell. 2022;185(13):2292–2308.e20. doi: 10.1016/j.cell.2022.05.021

[64] Dasanu CA. Length of adjuvant imatinib therapy in GIST: weighing benefits, side effects and costs. J Oncol Pharm Pract. 2012;18 (3):379–380. doi: 10.1177/1078155212453606

[65] Bouitbir J, Panajatovic MV, Krähenbühl S. Mitochondrial toxicity associated with imatinib and sorafenib in isolated rat heart fibers and the Cardiomyoblast H9c2 cell line. IJMS. 2022;23(4):2282. doi: 10.3390/ijms23042282

[66] Burda P, Hlavackova A, Polivkova V, et al. The rate of cellular energy production of muscle cells is attenuated by carnitine intracellular deficiency caused by imatinib treatment. Blood. 2021;138 (Supplement 1):3609–3609. doi: 10.1182/blood-2021-152516

[67] Ran FA, Hsu PD, Wright J, et al. Genome engineering using the CRISPR-Cas9 system. Nat Protoc. 2013;8(11):2281–2308. doi: 10.1038/nprot.2013.143

[68] Zheng Y, Wang L, Liu Q, et al. Modulation of virus-induced neuroinflammation by the autophagy receptor SHISA9 in mice. Nat Microbiol. 2023;8(5):958–972. doi: 10.1038/s41564-023-01357-3

[69] Zhang C-S, Hawley SA, Zong Y, et al. Fructose-1,6-bisphosphate and aldolase mediate glucose sensing by AMPK. Nature. 2017;548 (7665):112–116. doi: 10.1038/nature23275